ARMY RESEARCH LABORATORY

Failure Analysis of an AH-64 Main Rotor Damper Blade Rod End, P/N 7-211411186-5

by Scott M. Grendahl and Marc S. Pepi

ARL-TR-3100 December 2003

NOTICES

Disclaimers

The findings in this report are not to be construed as an official Department of the Army position unless so designated by other authorized documents.

Citation of manufacturer's or trade names does not constitute an official endorsement or approval of the use thereof.

DESTRUCTION NOTICE—Destroy this report when it is no longer needed. Do not return it to the originator.

Army Research Laboratory
Aberdeen Proving Ground, MD 21005-5069

ARL-TR-3100 **December 2003**

Failure Analysis of an AH-64 Main Rotor Damper Blade Rod End, P/N 7-211411186-5

Scott M. Grendahl and Marc S. Pepi
Weapons and Materials Research Directorate, ARL

REPORT DOCUMENTATION PAGE

Form Approved
OMB No. 0704-0188

1. REPORT DATE *(DD-MM-YYYY)*	2. REPORT TYPE	3. DATES COVERED (From - To)
December 2003	Final	January 2001 to October 2001

4. TITLE AND SUBTITLE

Failure Analysis of an AH-64 Main Rotor Damper Blade Rod End, P/N 7-211411186-5

5a. CONTRACT NUMBER

5b. GRANT NUMBER

5c. PROGRAM ELEMENT NUMBER

6. AUTHOR(S)

Scott M. Grendahl,; Marc S. Pepi (both of ARL)

5d. PROJECT NUMBER

184W41

5e. TASK NUMBER

5f. WORK UNIT NUMBER

7. PERFORMING ORGANIZATION NAME(S) AND ADDRESS(ES)

U.S. Army Research Laboratory
Weapons and Materials Research Directorate
Aberdeen Proving Ground, MD 21005-5069

8. PERFORMING ORGANIZATION REPORT NUMBER

ARL-TR-3100

9. SPONSORING/MONITORING AGENCY NAME(S) AND ADDRESS(ES)

10. SPONSOR/MONITOR'S ACRONYM(S)

11. SPONSOR/MONITOR'S REPORT NUMBER(S)

12. DISTRIBUTION/AVAILABILITY STATEMENT

Approved for public release; distribution is unlimited.

13. SUPPLEMENTARY NOTES

14. ABSTRACT

The U.S. Army Aviation and Missile Command asked the U.S. Army Research Laboratory's Weapons and Materials Research Directorate to determine the probable cause of cracking of an AH-64 main rotor damper blade rod end, part number 7-211411186-5. The component secures an end of one of the linkages on the helicopter's main rotor. The failure was noted while the helicopter was stationed in Seckenheim, Germany, on 10 June 1998. The investigation included visual examination, scanning electron microscopy, energy dispersive spectroscopy, hardness testing, chemical analysis, and retained austenite analysis. The analysis was conducted to evaluate whether the failure was an isolated event or part of an extensive problem in the fleet.

15. SUBJECT TERMS

failure analysis inter-granular corrosion PH15-5, 440C

16. SECURITY CLASSIFICATION OF:			17. LIMITATION OF ABSTRACT	18. NUMBER OF PAGES	19a. NAME OF RESPONSIBLE PERSON
a. REPORT	b. ABSTRACT	c. THIS PAGE			Scott M. Grendahl
UNCLASSIFIED	UNCLASSIFIED	UNCLASSIFIED	UL	60	19b. TELEPHONE NUMBER (*Include area code*) 410-306-0819

Standard Form 298 (Rev. 8/98)
Prescribed by ANSI Std. Z39.18

Contents

List of Figures

List of Tables

1. Background

The U.S. Army Aviation and Missile Command asked the U.S. Army Research Laboratory's (ARL's) Weapons and Materials Research Directorate to determine the probable cause of cracking of an AH-64 main rotor damper blade rod end, Part Number 7-211411186-5. The part, situated along the main rotor hub in the position denoted on figure 1, had 353 service hours since installation, and the ball portion was discovered cracked during a routine inspection. The failure was noted while the helicopter was stationed in Seckenheim, Germany, on 10 June 1998. The part was received by ARL on 24 July 1998.

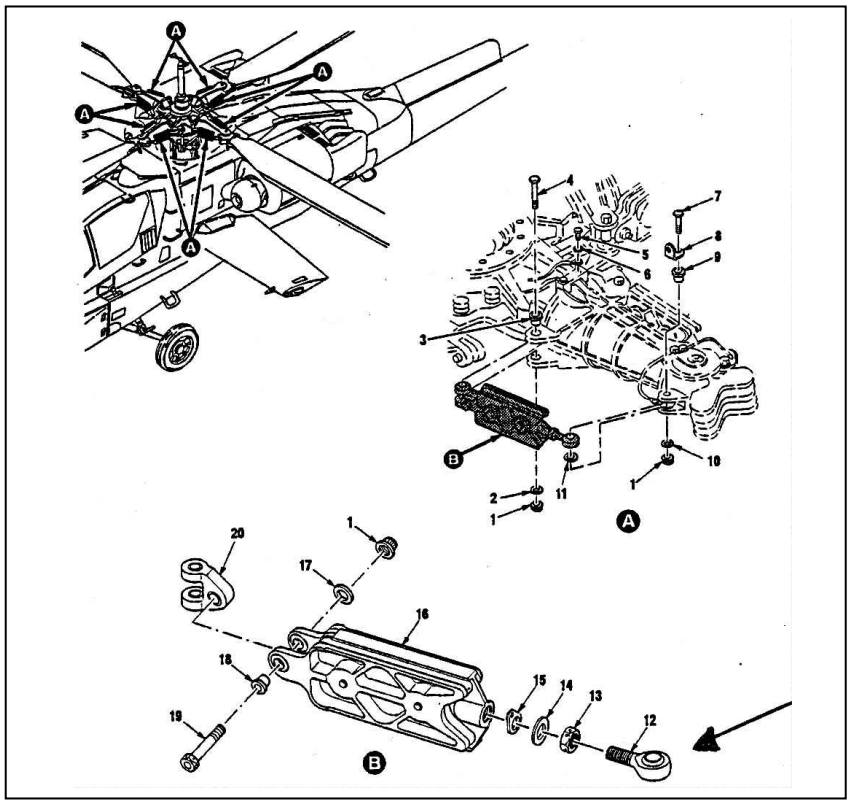

Figure 1. Schematic of component location on the aircraft.

2. Material/Specification Requirements

The main rotor damper blade rod end consists of three separate components: a body, a plastic-lined outer ring, and a ball. The following list outlines the material requirements for each of these components:

Body: 15-5 PH[1] corrosion-resistant steel (CRES) per Aerospace Material Specification (AMS) 5659, condition H1025, Rockwell C Hardness (HRC) 35-42 per HP1-17[2].

Outer Ring: 15-5 PH CRES steel per AMS 5659, condition H1150, HRC 28-37 per HP1-17.

Ball: 440C CRES per AMS 5630, heat-treated HRC 55 minimum per HP1-1.

Liner: Karon H, Teflon[3] fabric or equivalent.

3. Heat Treatment

The ball is required to be heat treated as dictated by McDonnell Douglas Specification HP 1-1, listed in table 1.

Table 1. Heat treatment requirement for 440C CRES ball

Annealing °F (°C)		**Transformation Hardening Cycle °F (°C)**		**Approximate Tempering**
Temp.	Furnace Cool to Approx. Temp. Shown	Austenitizing Temp.	Quenchant	Temp. °F (°C)
1,550 to 1,600 (843 to 871) for 6 hours or 1,650 (899) for 2 hours plus 1,300 (704) for 4 hours	25 to 50 (14 to 28) per hour to 1,100 (593)	1,900 to 1,950 (1,038 to 1,066)	Oil	450 (232) for 55 HRC min.

*Note: The "quench" for 440C steel shall be followed by refrigeration at -110+10/-40° F (-79+6/-40° C) for 2 hours minimum. The cooling treatment shall be performed immediately after quenching. Double tempering is required.

4. Visual Examination/Light Optical Microscopy

The failed part is shown in figure 2 in the as-received condition (approximately 1x magnification). The ball component of the assembly contained a "through" (i.e., complete) crack that was observed along the exterior as well as the interior (see figure 3). The body and the outer ring were sectioned by ARL in order to extract the cracked ball. Special care was taken not to damage the crack. Figures 4 and 5 show both halves of the cracked ball. One half of the ball, subsequently labeled "A" (see figure 4), was cleaned in an Alconox solution to remove the

[1] precipitation hardenable

[2] an internal Boeing specification

[3] Teflon® is a registered trademark of E.I. DuPont de Nemours & Co., Inc.

coarse corrosion products. After cleaning, evidence of beach marks (i.e., groups of fatigue striations) became apparent, as well as the fracture origin indicated by the arrow.

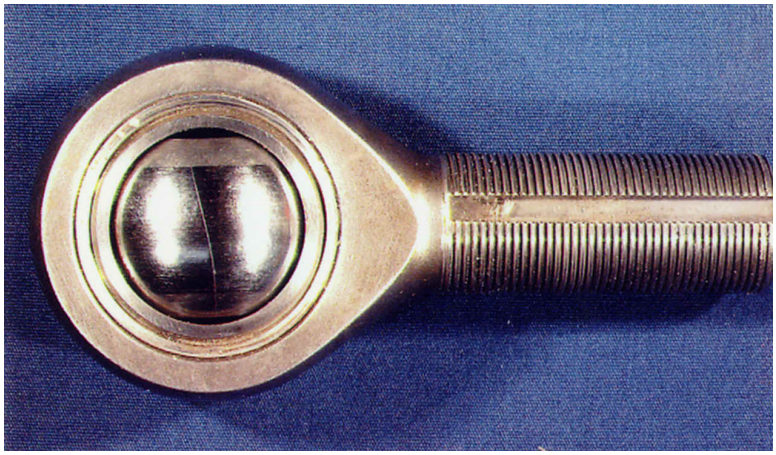

Figure 2. Failed component in the as-received condition (mag ~1x).

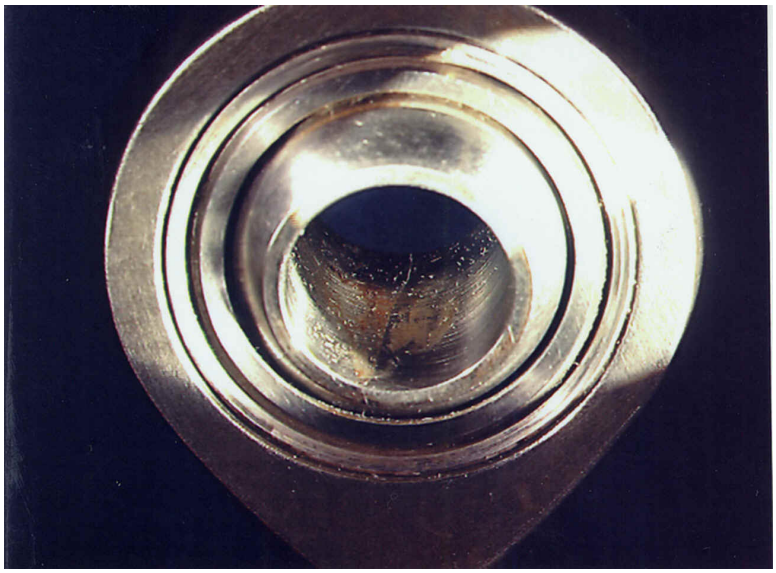

Figure 3. Through crack visible along the interior bore (mag ~2x).

Figure 5 shows half "B," which remained in the as-received condition for further analysis (see SEM/EDS section 9).

Off-axis views of the ball halves are presented in figures 6 and 7 to detail the corrosion observed along the internal bore of the ball near the through crack. This corrosion may have formed after the crack propagated entirely through the ball.

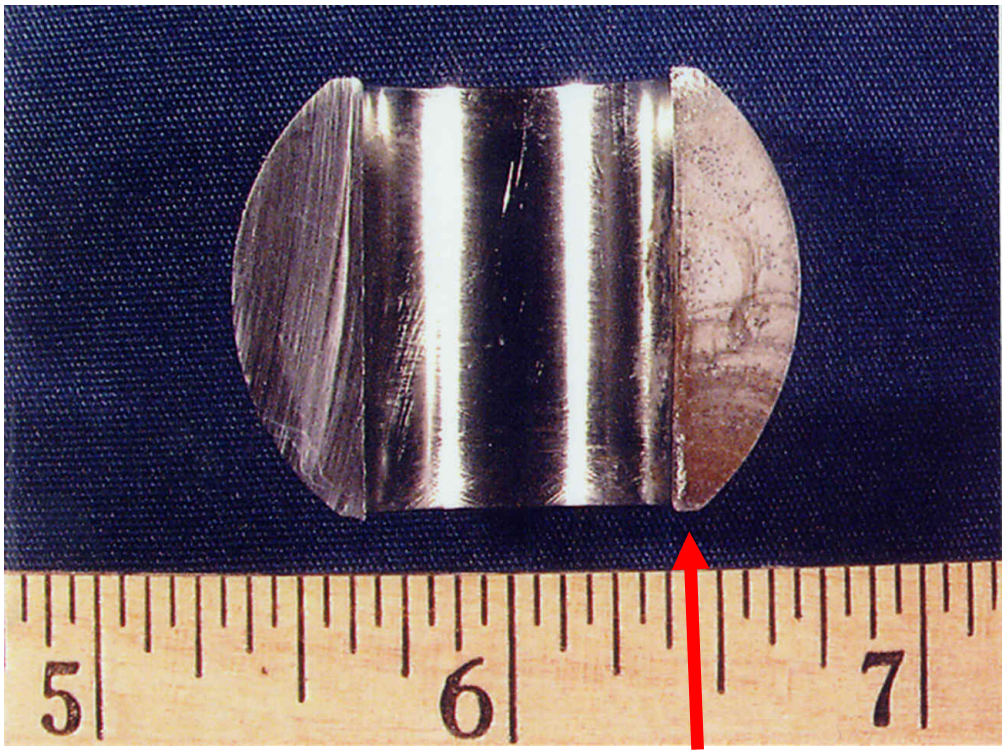

Figure 4. Fracture half "A" cleaned in an Alconox solution (scale in inches).

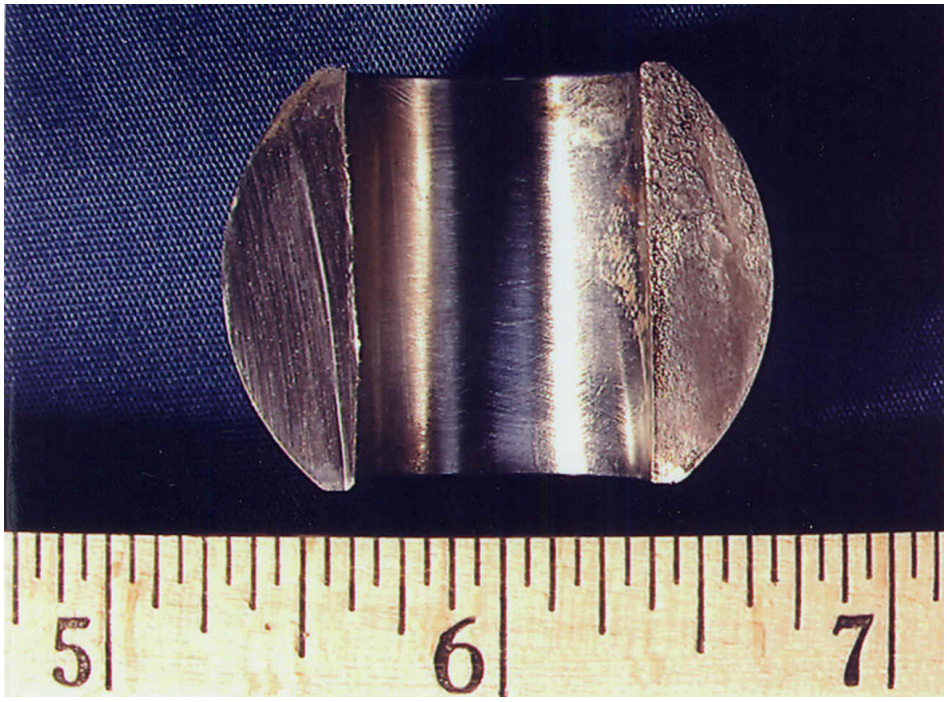

Figure 5. Fracture half "B," left in the as-received condition (scale in inches).

Figure 6. Fracture half "A" showing corrosion along the inside bore (mag ~2x).

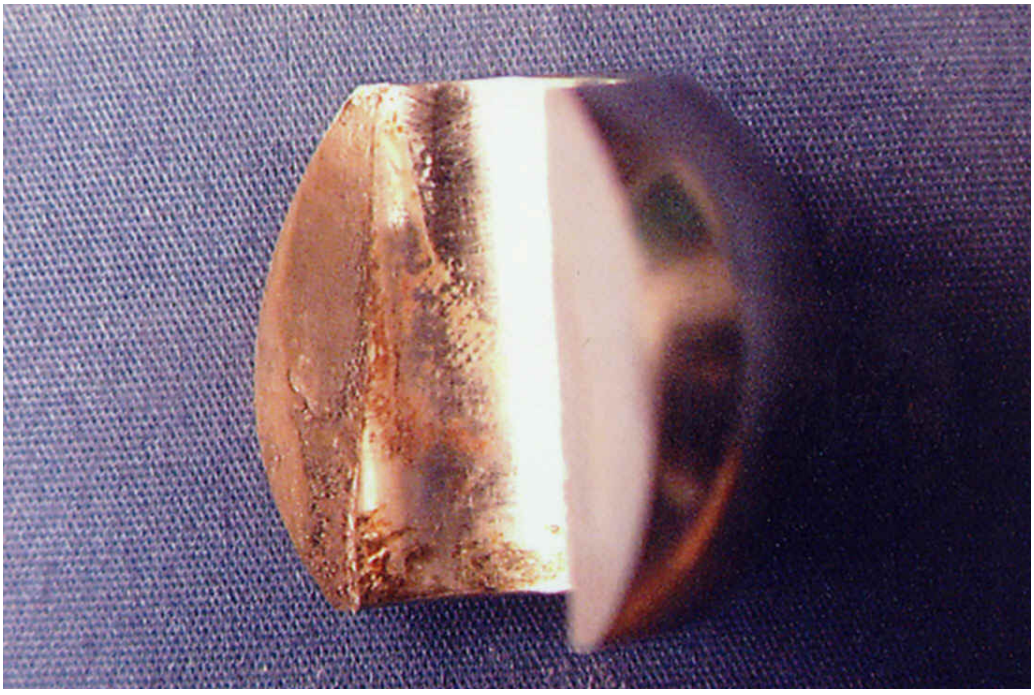

Figure 7. Fracture half "B" depicting corrosion along the inside bore (mag ~2x).

Figure 8 depicts the fracture origin from half "A". Note the progressive, distinct beach marks emanating outward from the origin, which indicate fatigue crack propagation. The fracture propagated on a relatively flat plane until approximately one-quarter into the cross-sectional area

of the ball; thereafter cracking occurred on different planes. Separate distinct beach marks can be observed at the halfway point and again at the three-quarters position.

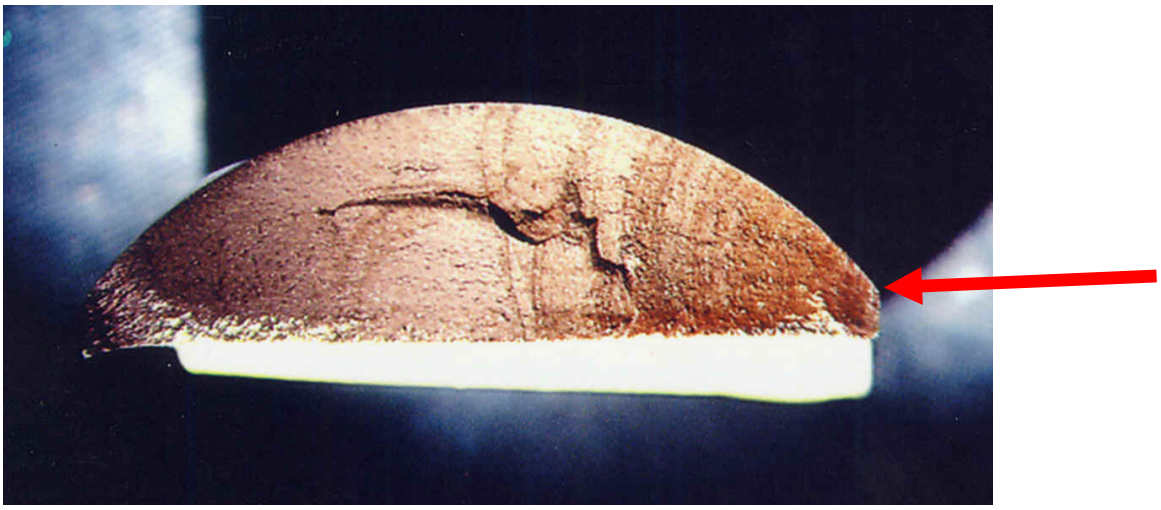

Figure 8. Fracture half "A" detail, two distinct fracture planes (mag ~2x).

Further examination of fracture half "A" revealed numerous corroded areas, as shown in figures 9 through 11. The areas of attack were approximately 0.19, 0.04, and 0.01 inch from the origin. Figure 12 depicts the sites in figure 11 at higher magnification to show detail more clearly.

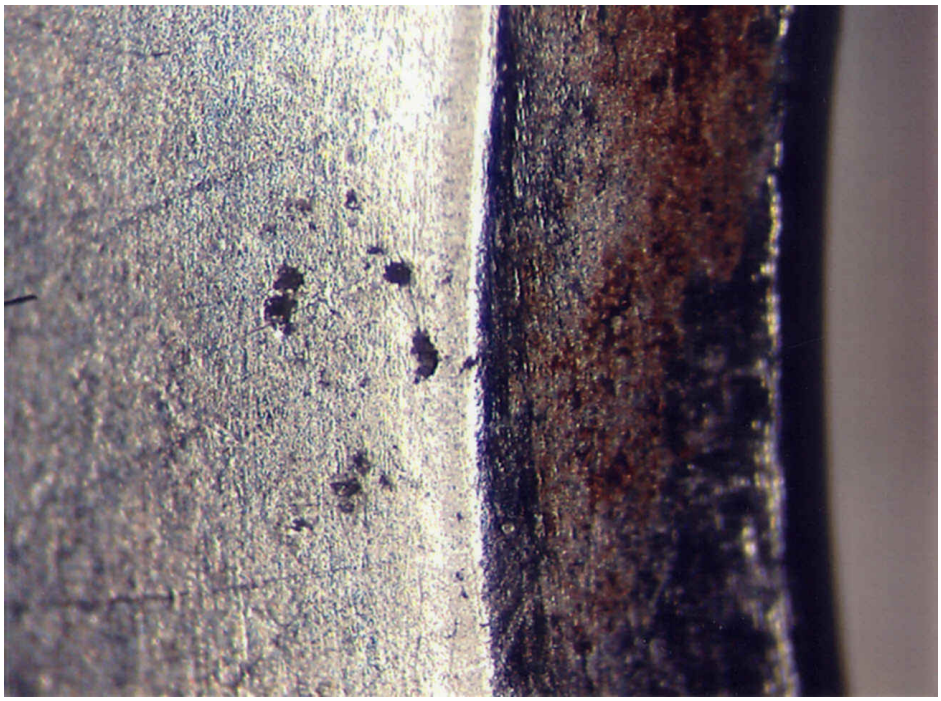

Figure 9. Corroded areas near fracture origin (mag ~30x).

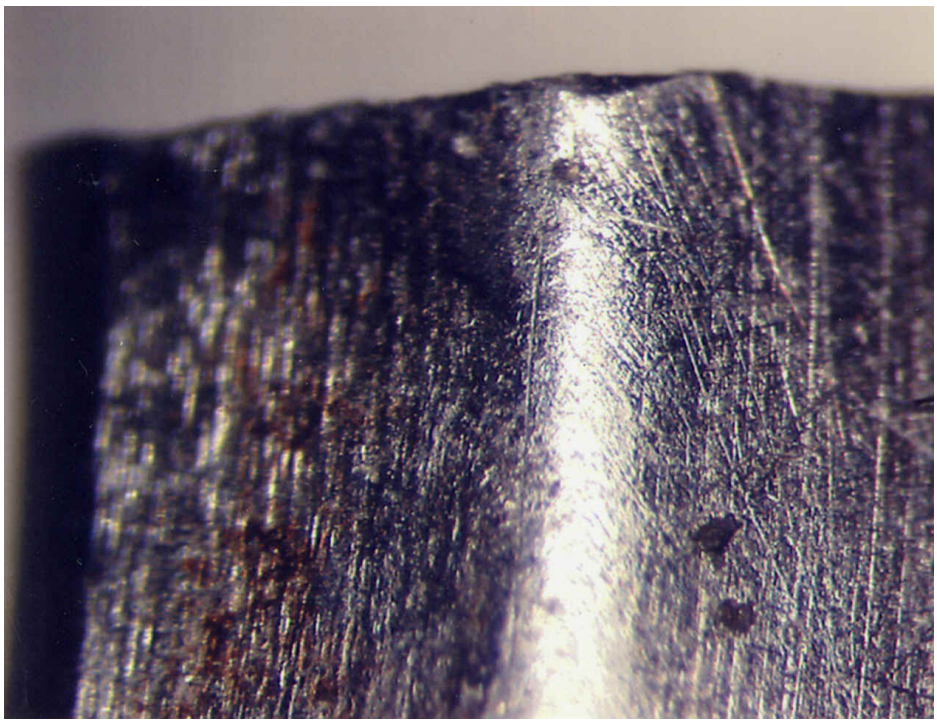

Figure 10. Attacked areas near origin of fracture (mag ~50x).

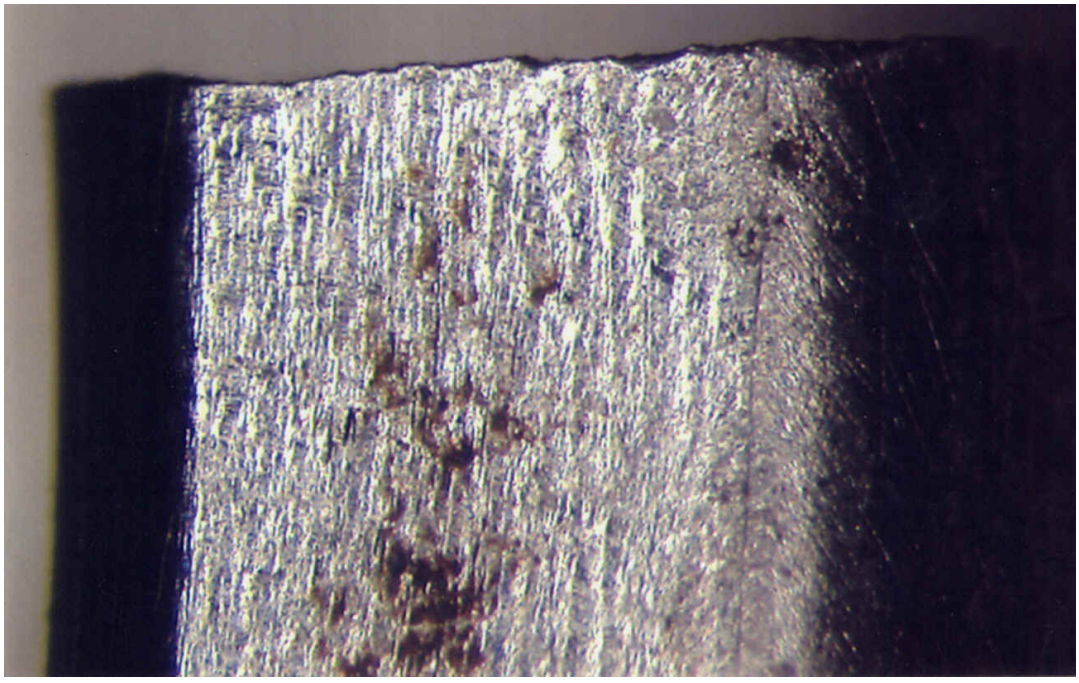

Figure 11. Corrosion on chamfered edge adjacent to fracture plane (mag ~40x).

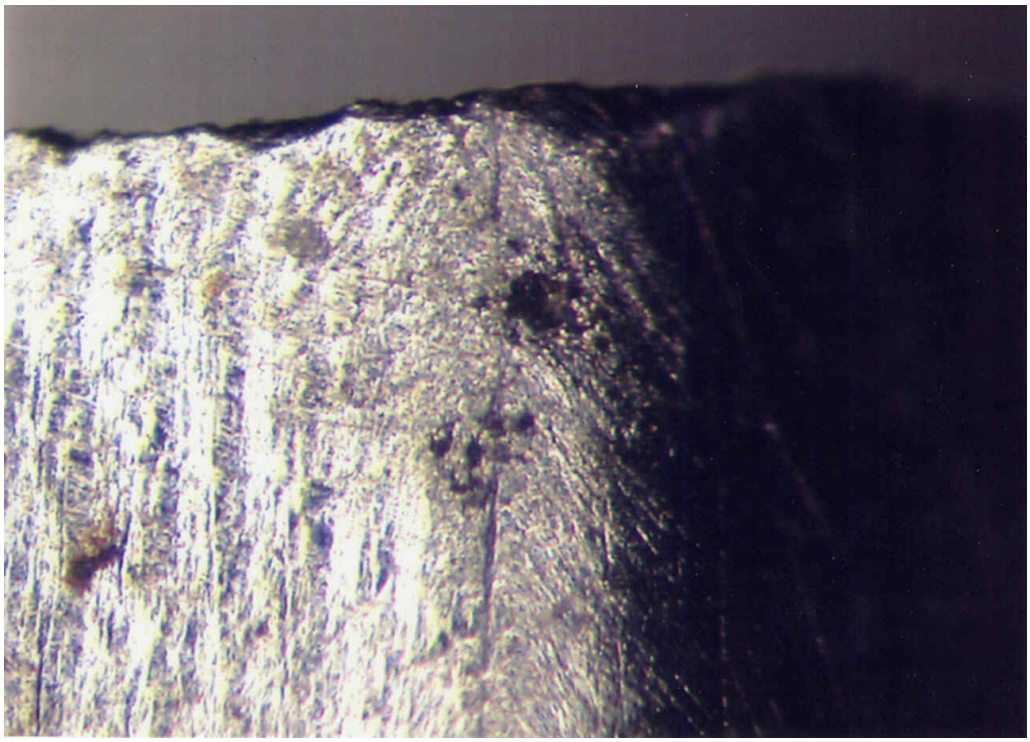

Figure 12. Detail of Figure 11 showing localized corrosion near origin (mag ~100x).

The corroded regions were uniform in neither size nor frequency. Light optical examination only revealed this condition on the exterior surface of the ball. The interior bored hole through the ball was noticeably void of these areas of corrosion. Less than 5% of the exterior surface of the ball contained corrosion. Examination of the "B" fracture half revealed similar features as those noted on half "A". In addition, significant secondary cracking was observed, which ran parallel to the fracture plane. One crack was 0.21 inch from the fracture plane and was more than 0.125 inch long, as shown in figure 13. Figure 14 shows the presence of a slightly smaller crack adjacent to the crack shown in figure 13.

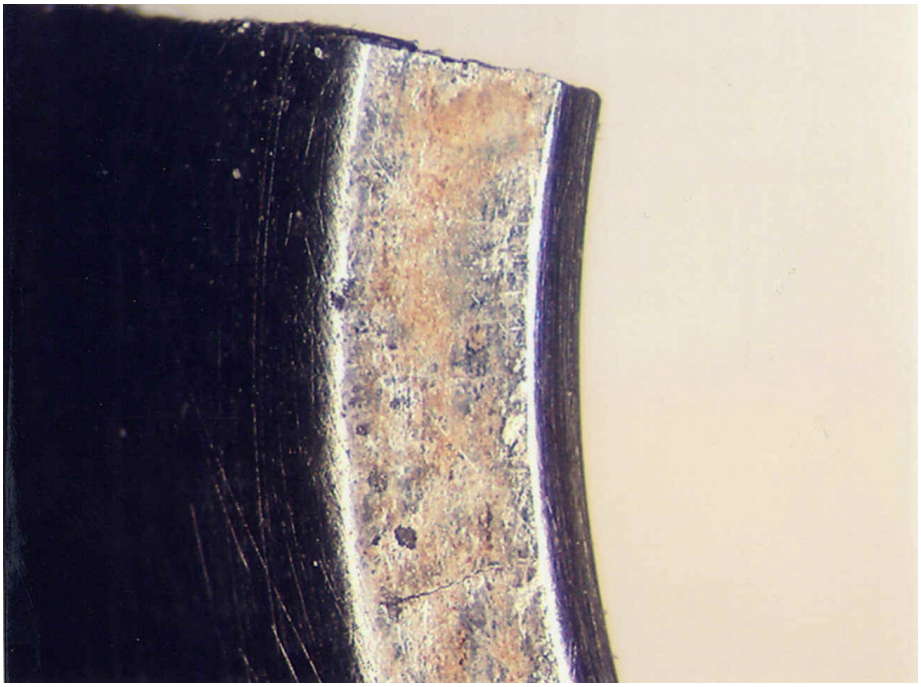

Figure 13. Secondary crack noted adjacent to the fracture plane (mag ~20x).

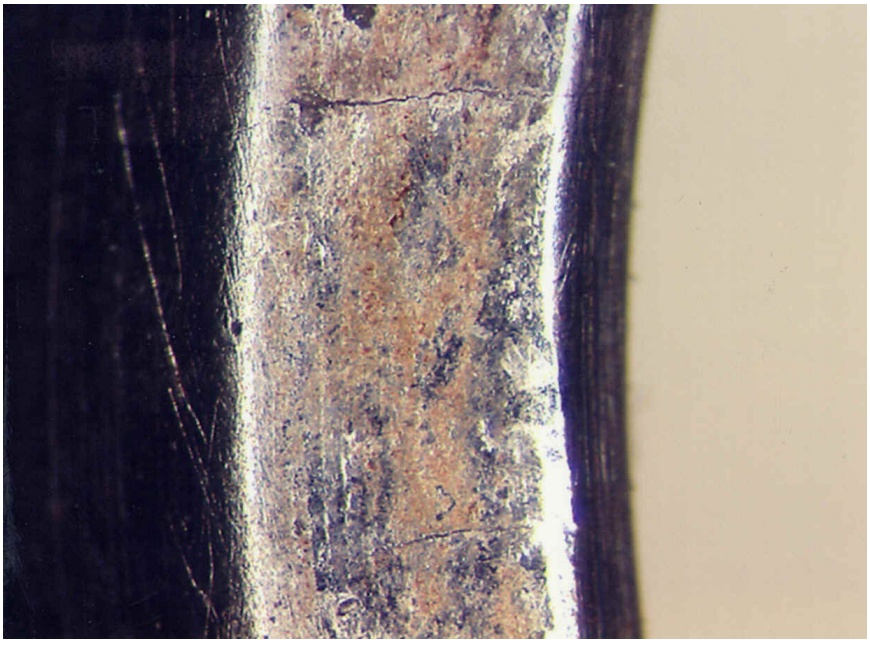

Figure 14. Small secondary crack adjacent to fracture plane (mag ~30x).

5. Chemical Analysis

A section of the material was subjected to chemical analysis to determine the elemental composition of the alloy. The carbon content was determined through combustion infrared detection, while sulfur was revealed through combustion automatic titration. The percentages of the remaining elements were determined through direct coupled plasma emission spectroscopy. Table 2 presents the results of this analysis. The results showed that the component conformed to the required chemical composition.

Table 2. Chemical composition - weight percent type 440C stainless steel

Element	Component	Requirement (AMS 5630)
Carbon	1.01	0.95 - 1.20
Manganese	0.39	1.00 max.
Silicon	0.75	1.00 max.
Phosphorus	0.016	0.040 max.
Sulfur	0.005	0.030 max.
Chromium	16.85	16.00 - 18.00
Molybdenum	0.48	0.40 - 0.65
Nickel	0.13	0.75 max.
Copper	0.035	0.50 max.
Cobalt	0.027	-
Vanadium	0.029	-
Iron	remainder	remainder

6. Metallography

Longitudinal and transverse sections of the failed component were metallographically prepared with silicon carbide papers, ranging in grit from 120 to 600, followed by 12 and then 9 micron diamond, and finished with 0.05-micron alumina. The specimens were sectioned as shown in figure 15.

The specimens were examined in the as-polished condition. Localized regions of surface inter-granular attack were noted in the areas shown in figure 16. The corresponding measurements were approximated with simple geometry. Except for one very small region on the interior of the longitudinal sample (see figure 16), each region of attack was noted on the exterior surface of the part. It was interesting to note that the bulk of the inter-granular regions observed on the longitudinal sample corresponded to the general location of the fracture origin.

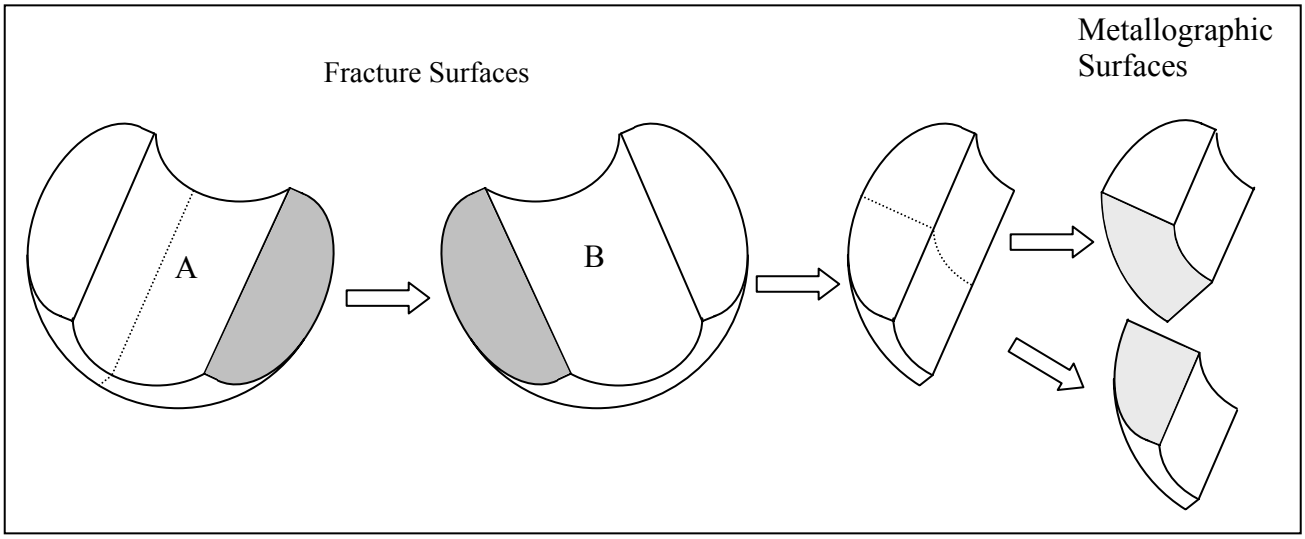

Figure 15. Sectioning schematic of the failed type 440C ball.

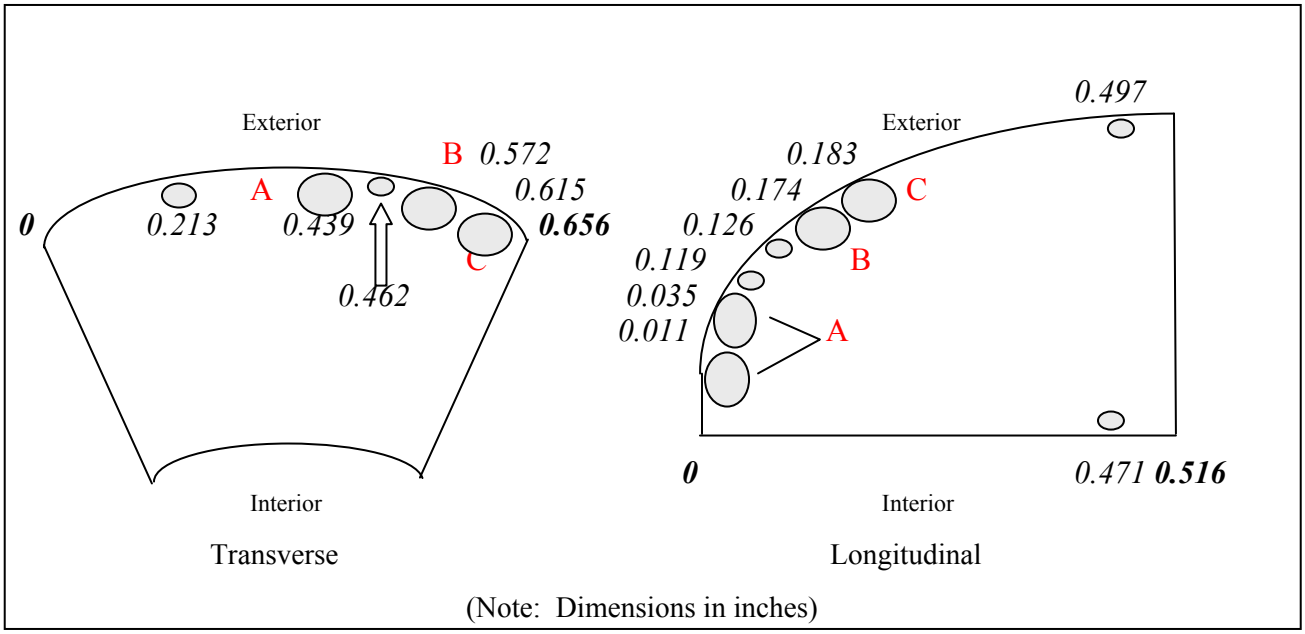

Figure 16. Schematic of localized inter-granular attacked locations.

The regions of attack labeled "A," "B," and "C" in figure 16 are shown in figures 17, 18, and 19 for the transverse section and in figures 20, 21, and 22 for the longitudinal section, respectively. In these photomicrographs, it is apparent that inter-granular cracks progressed to and around the precipitates (figures 17 and 21, especially). This fact is intuitive when it is realized that the matrix is inherently depleted of chromium in these areas. Figure 18 shows that individual grains of metal have actually been dislodged from the network of inter-granular attack, forming a cavity or pit at the surface of the part.

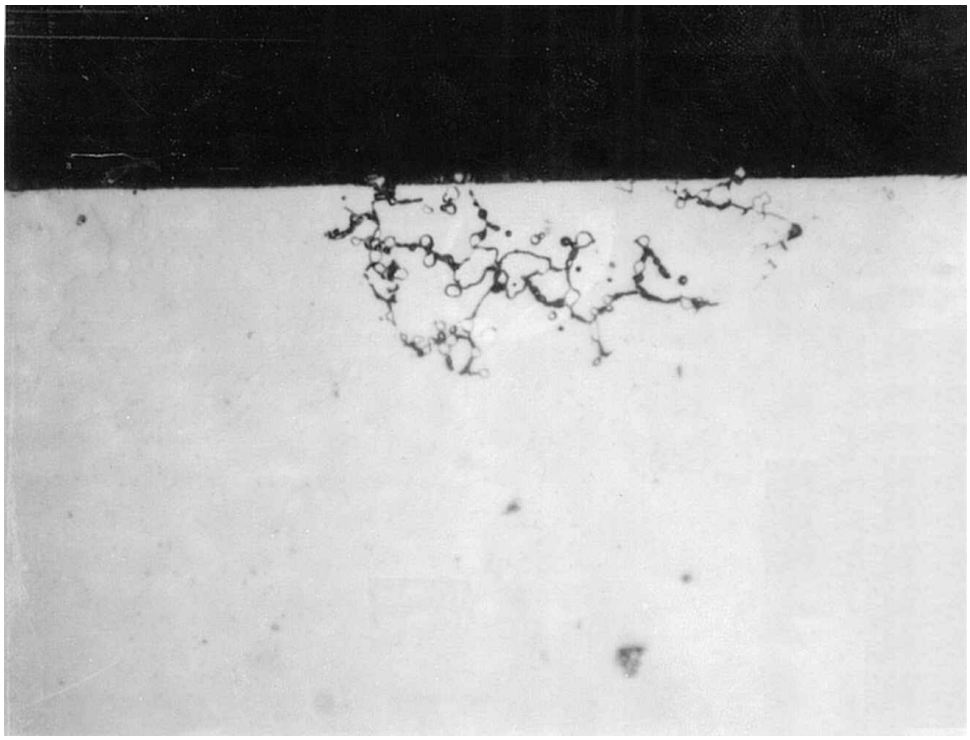

Figure 17. Transverse metallographic section area "A," unetched (mag 1kx).

Figure 18. Transverse metallographic section area "B," unetched (mag 500x).

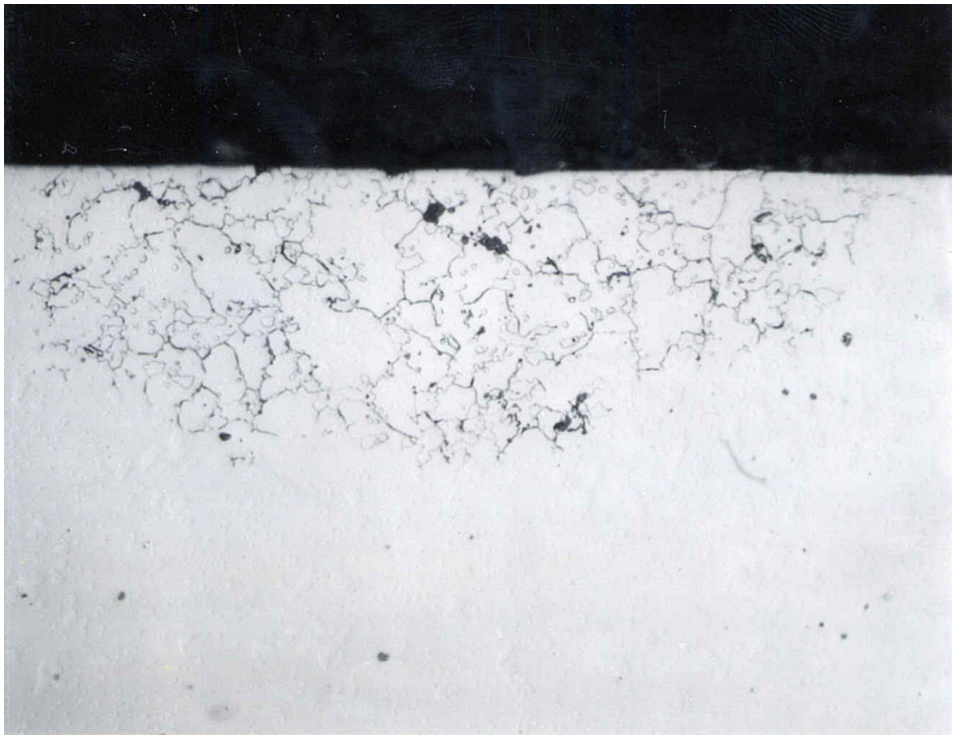

Figure 19. Transverse metallographic section area "C," unetched (mag 500x).

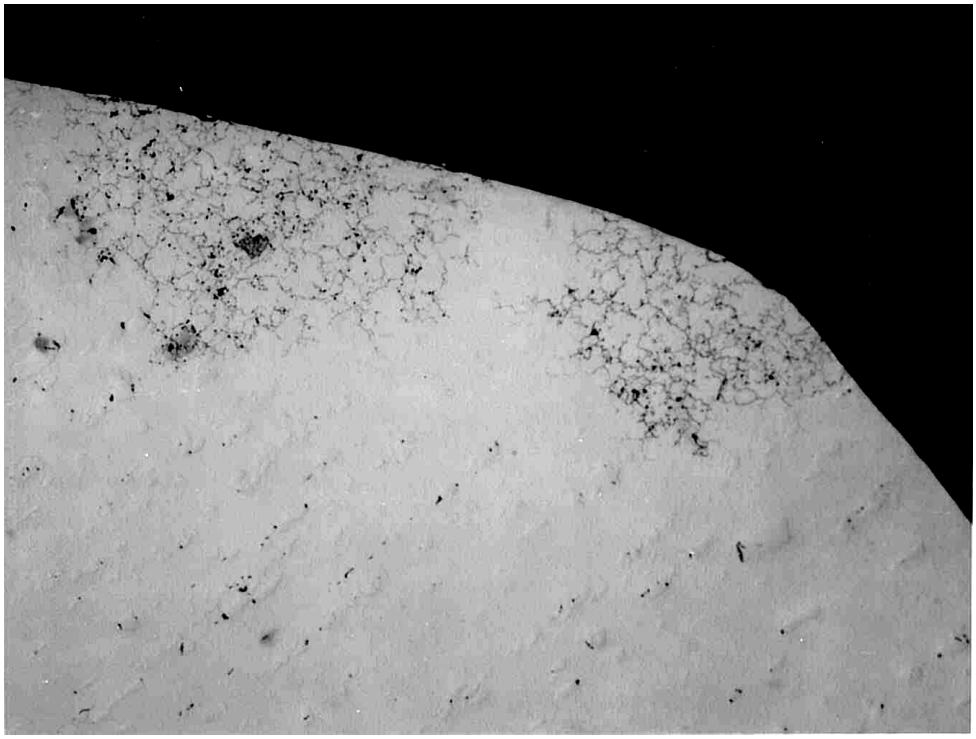

Figure 20. Longitudinal metallographic section area "A," unetched (mag 200x).

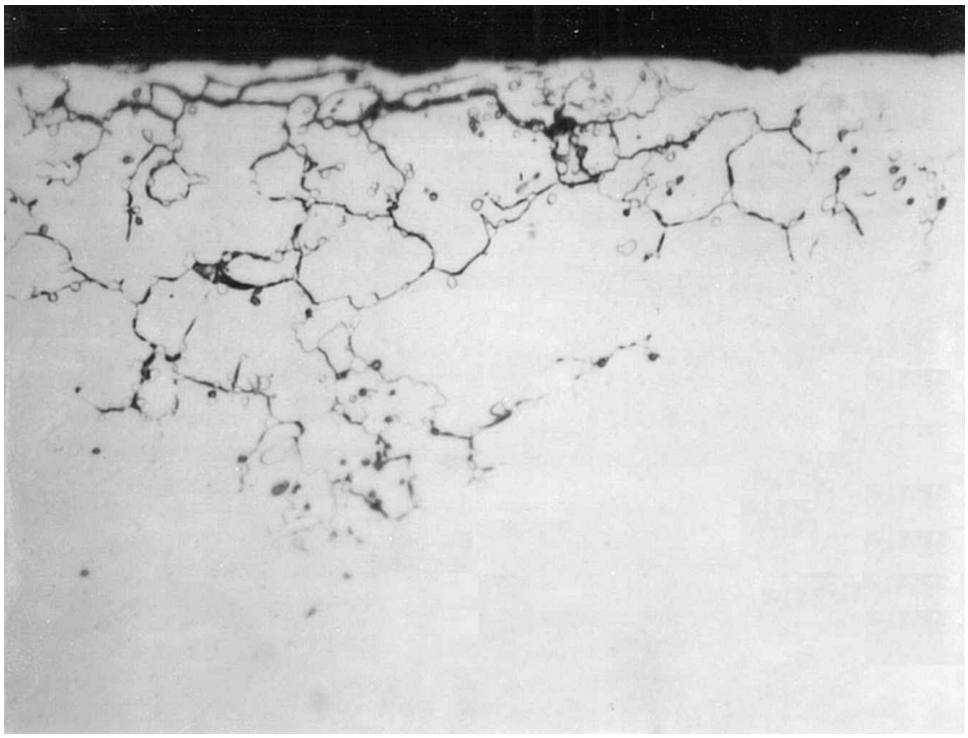

Figure 21. Longitudinal metallographic section area "B," unetched (mag 1kx).

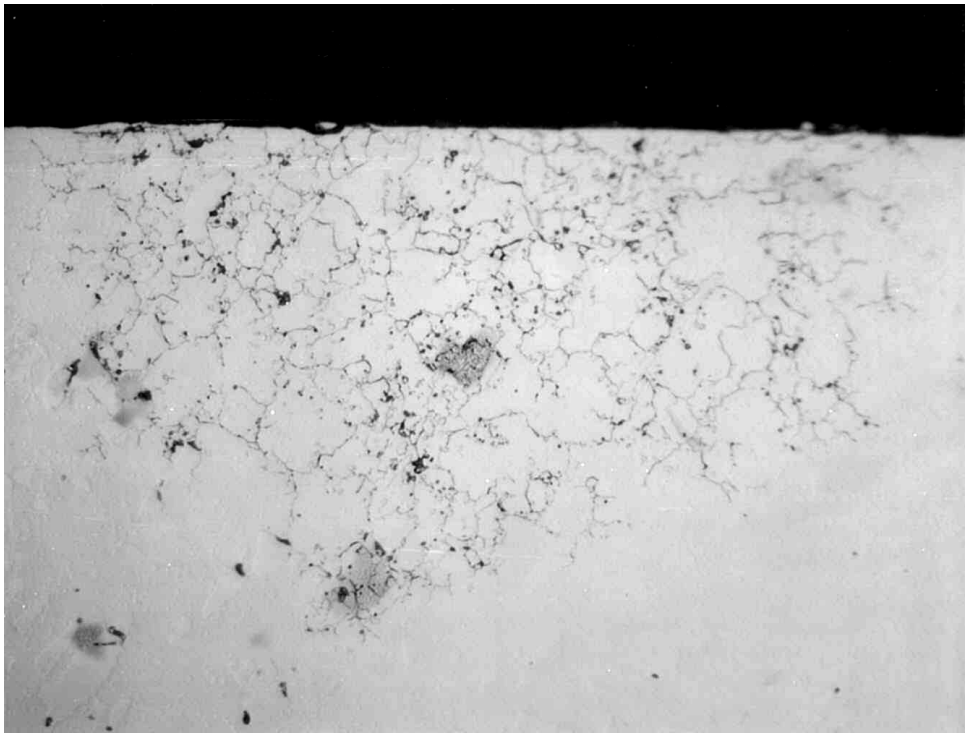

Figure 22. Longitudinal metallographic section area "C," unetched (mag 400x).

The samples were subsequently etched with Vilella's reagent to reveal the microstructural features. At low magnification, some banding was noted, indicative of the prior flow direction (see figure 23) in the material.

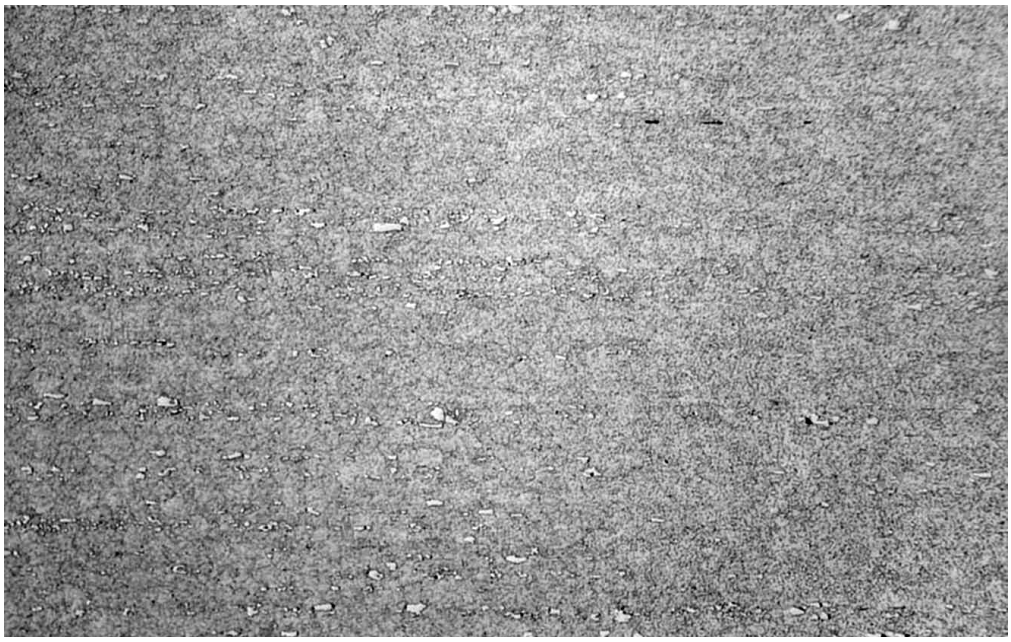

Figure 23. Etched microstructure of the ball material showing the presence of banding (mag 100x).

The grain size of the material was determined to be 8 or finer with the reticle overlay shown in figure 24. The regions of inter-granular attack were observed after the etchant was applied. Figures 25 through 30 correspond to the respective regions depicted in figures 17 through 22. The inter-granular nature of the attack became enhanced upon etching.

The microstructure was subsequently observed at 500x and 1000x magnification (see figures 31 and 32, respectively). The structure consisted of primary M_7C_3 carbides (figures 31a and 32a) and secondary carbides (small spheriodal particles shown in figures 31b and 32b) in a matrix of tempered martensite. Note, however, that Vilella's reagent does not reveal the tempered martensitic structure in this material as it appears in other common steels. The lathe-like structure is noticeably obscured. The primary carbides ranged in size, measuring as long as 0.0012 inch (30 μm). This size was well within the nominal size (as long as 60 μm) to be expected for this alloy. The structure was typical of type 440C stainless steel that has been austenitized, quenched, and tempered.

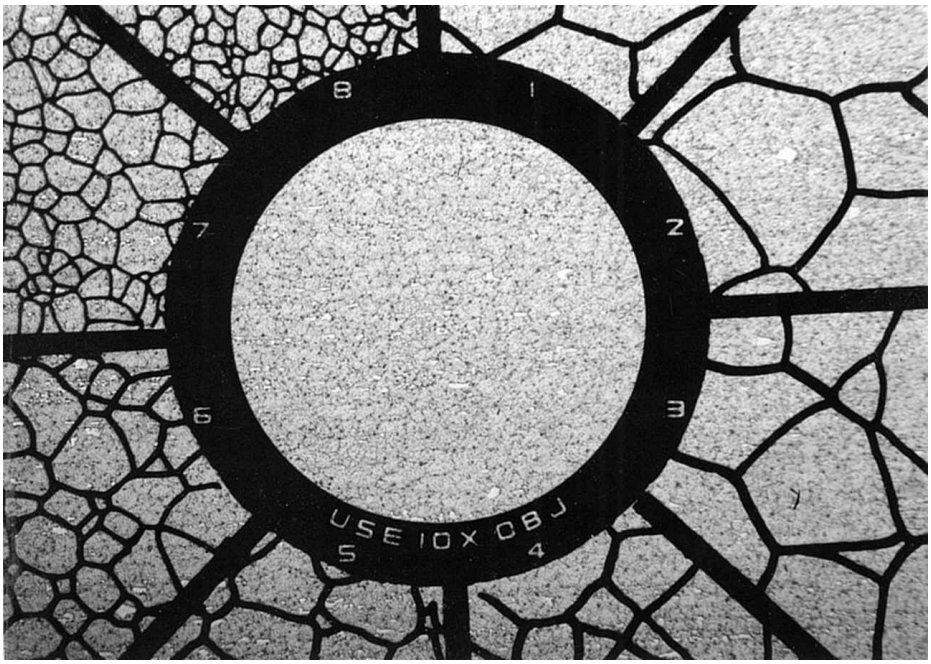

Figure 24. Etched microstructure demonstrating the grain size to be 8 or finer (mag 100x).

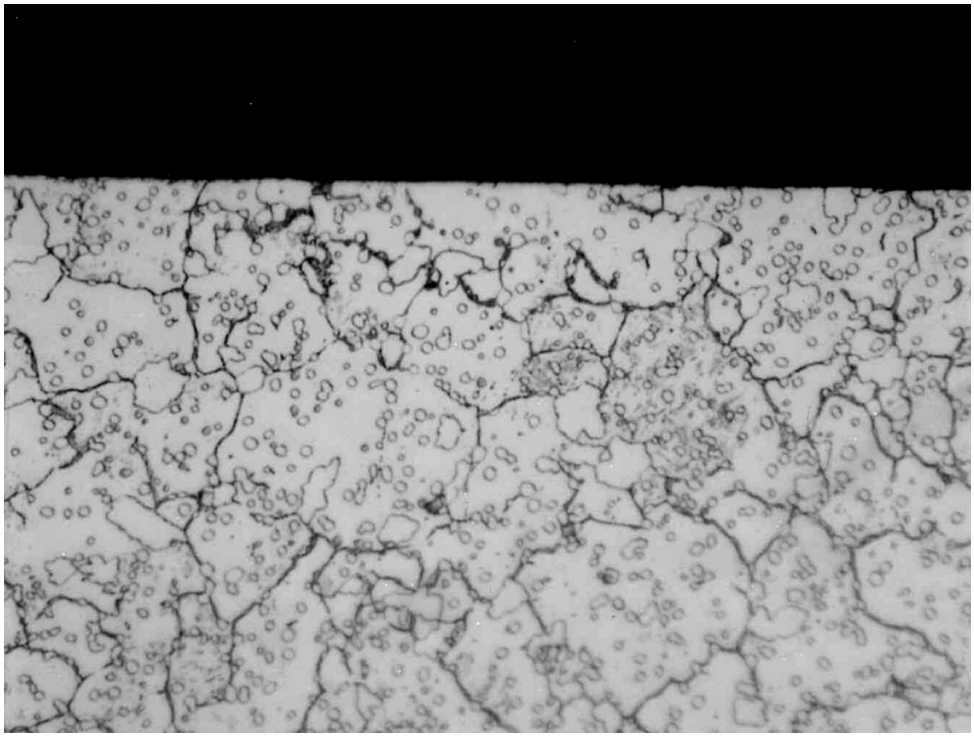

Figure 25. Etched transverse metallographic section area "A," (mag. 1kx).

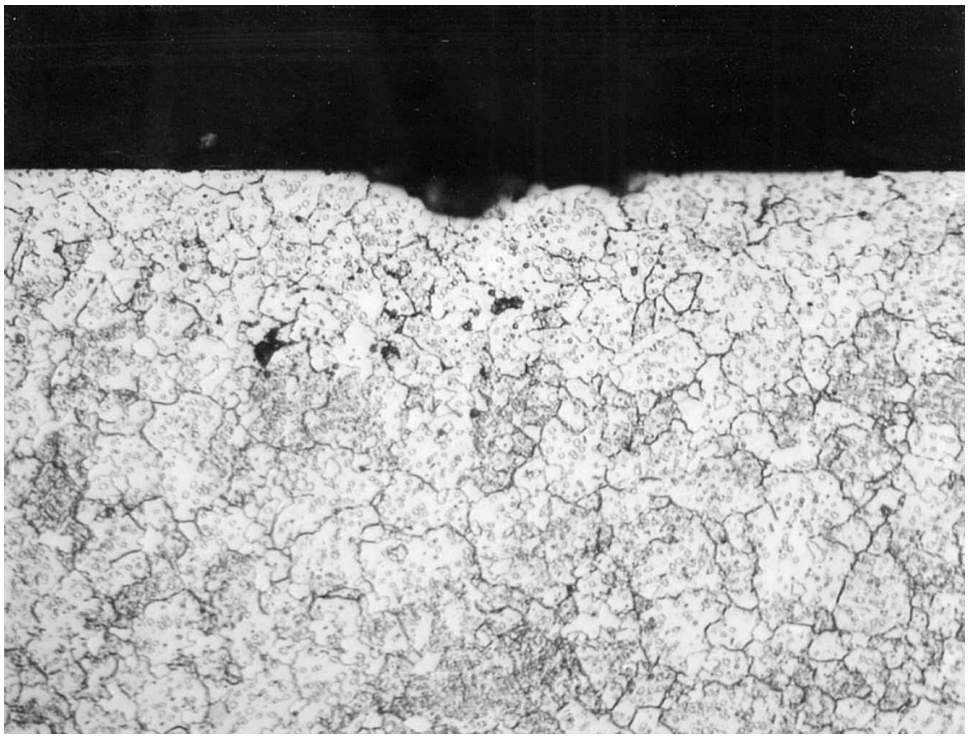

Figure 26. Etched transverse metallographic section area "B," (mag 500x).

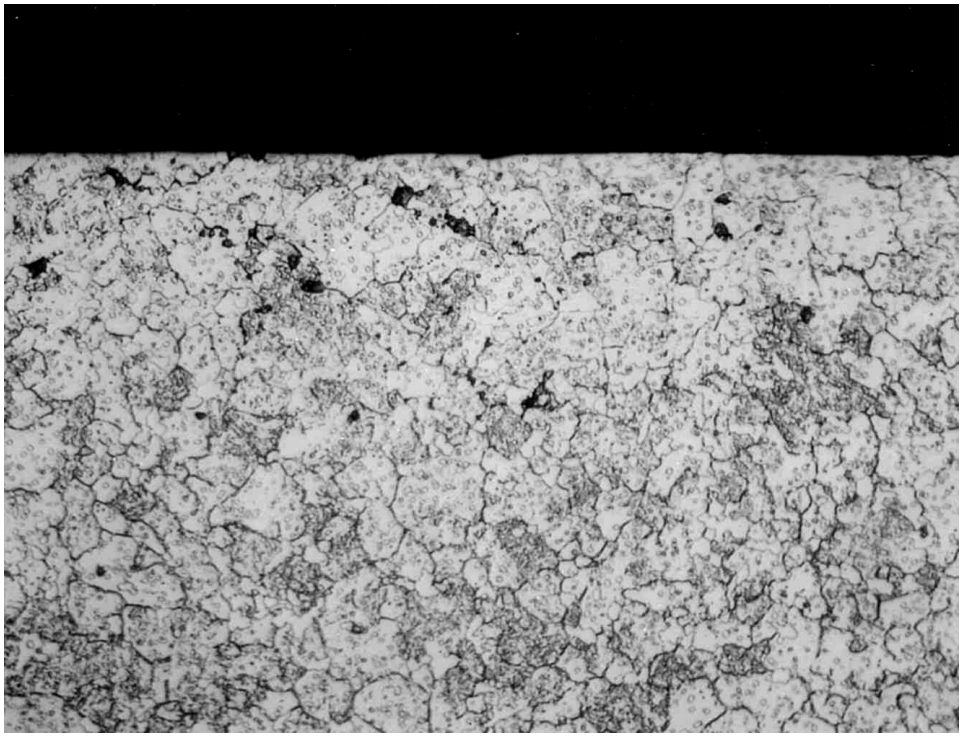

Figure 27. Etched transverse metallographic section area "C," (mag 500x).

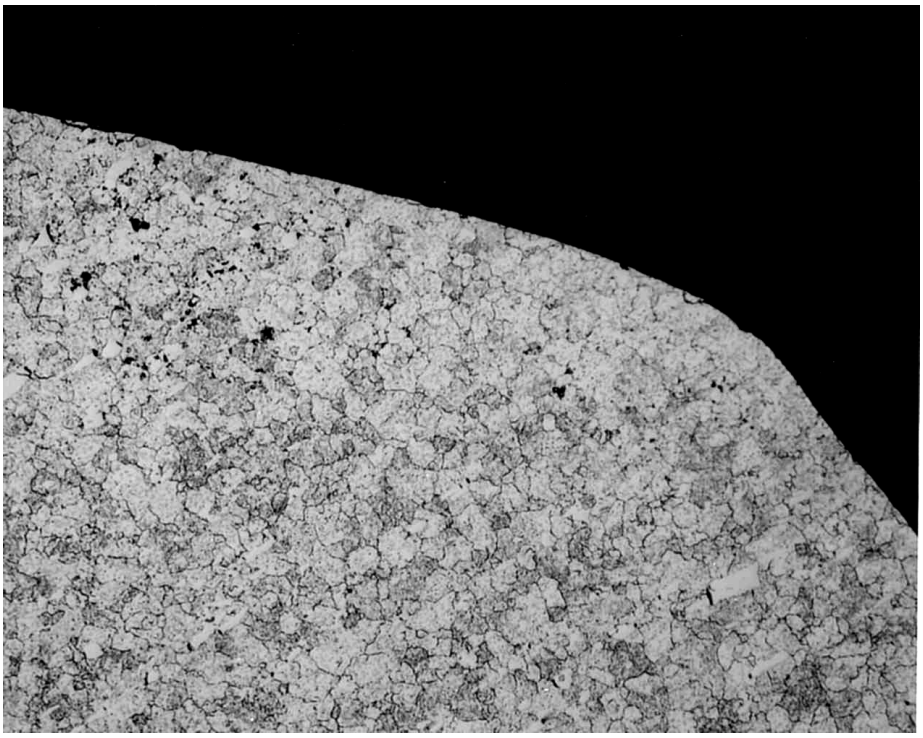

Figure 28. Etched longitudinal metallographic section area "A," (mag 200x).

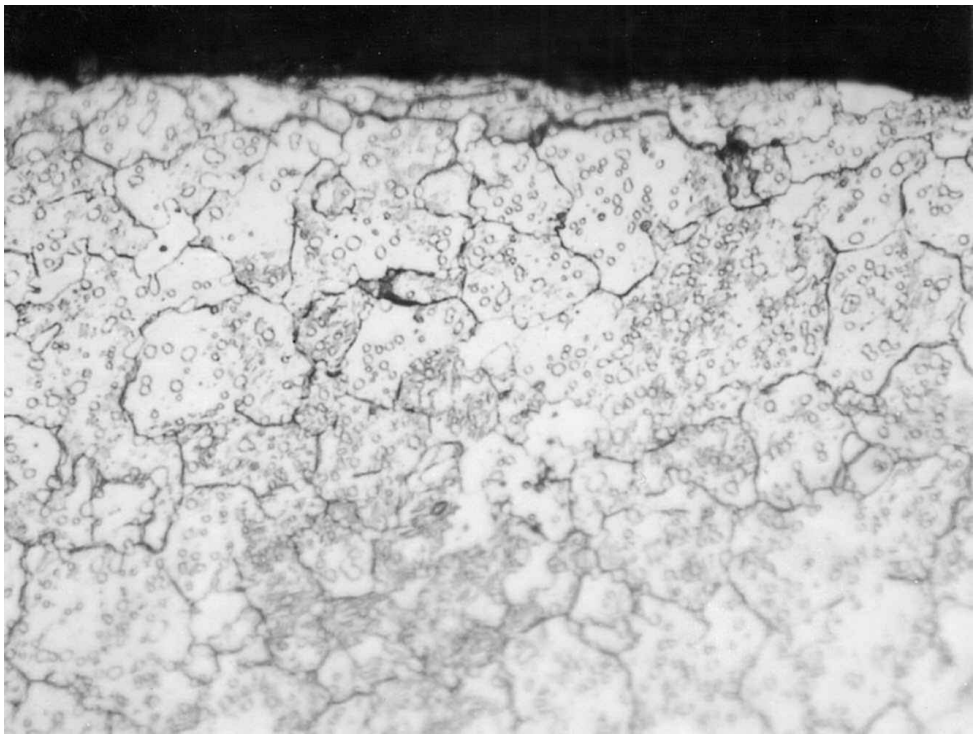

Figure 29. Etched longitudinal metallographic section area "B," (mag 1kx).

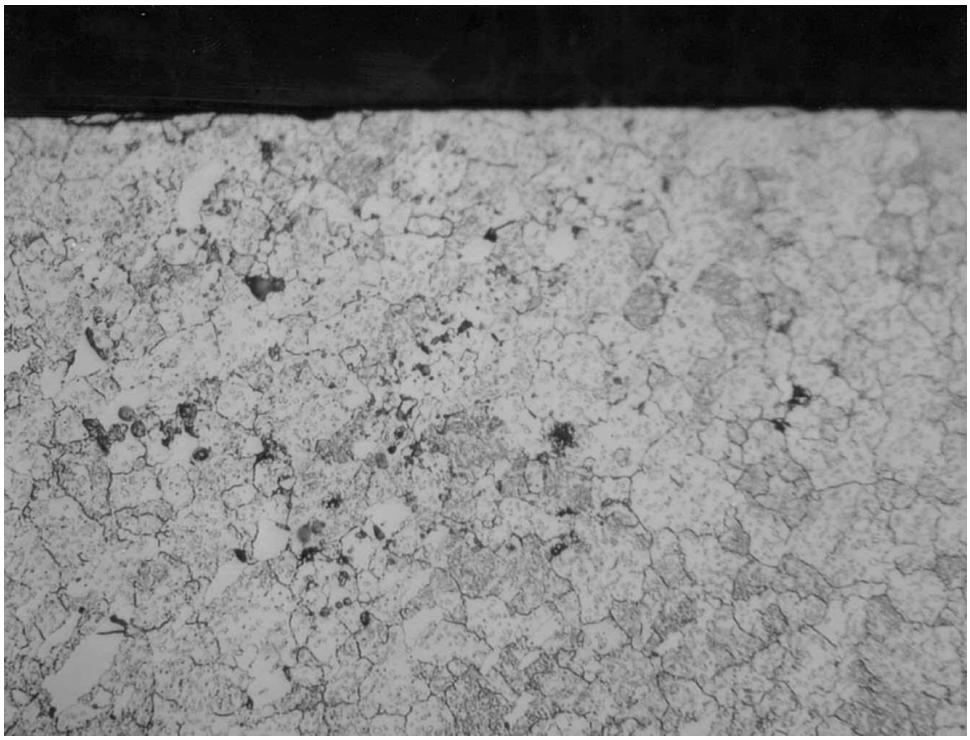

Figure 30. Etched longitudinal metallographic section area "C," (mag 400x).

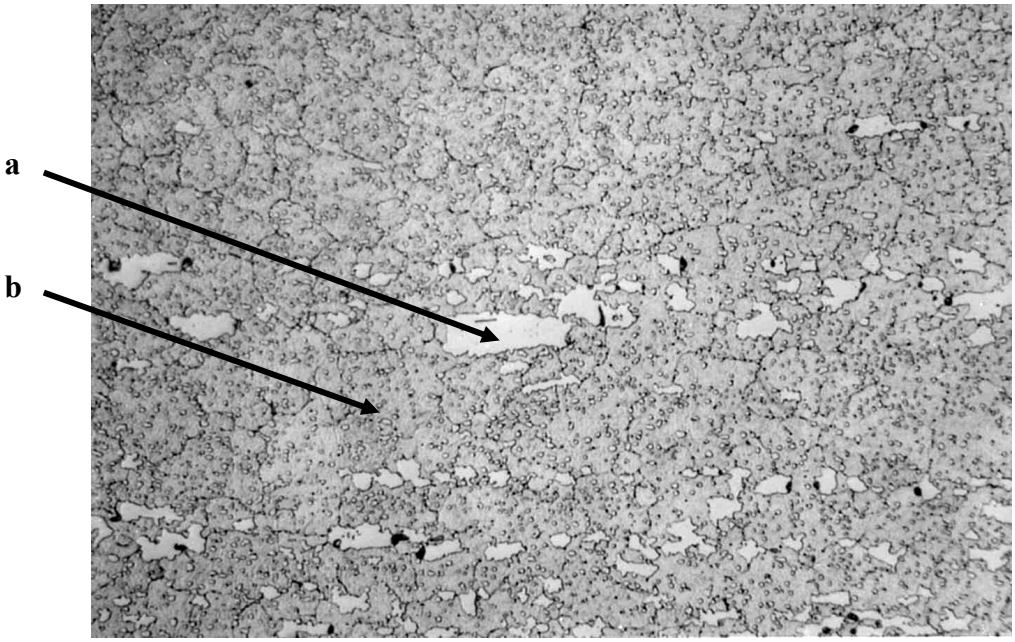

Figure 31. Etched longitudinal microstructure of 440C ball (mag 500x).

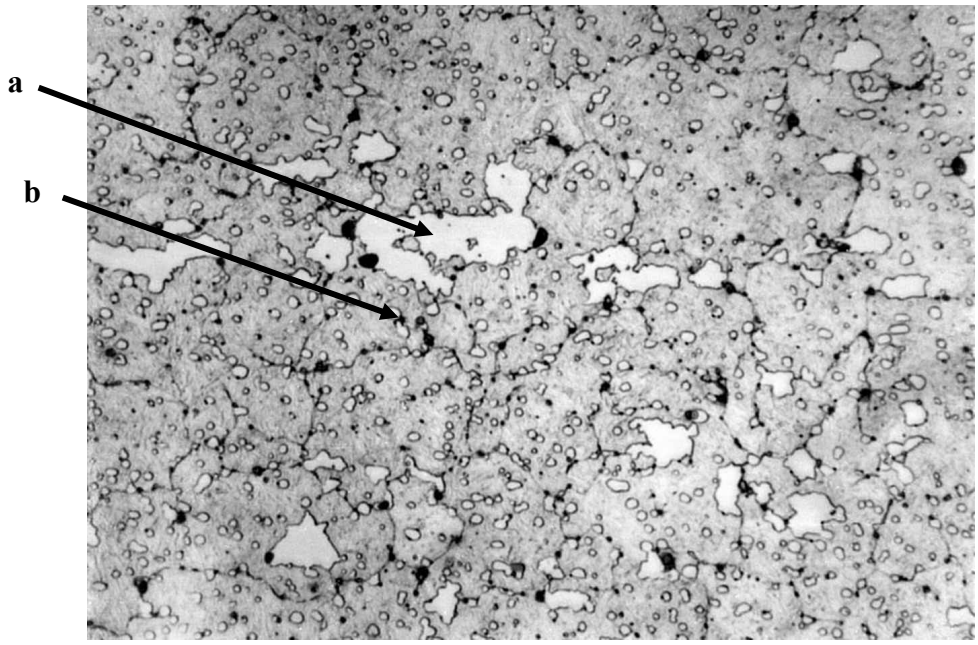

Figure 32. Etched longitudinal microstructure of 440C ball (mag 1kx).

7. Macro-Hardness Testing

The hardness of each of the three components that comprise the damper blade rod end was measured for conformance. Tables 3 through 5 list the results of hardness testing on the body, outer ring, and ball, respectively. The HRC was used on the body, while the HR15-N scale was used on the outer ring and the ball. These readings were subsequently converted to HRC readings via standard conversion charts. The HR15-N scale was used on the outer ring and ball because of the relatively small flat portion on these parts. This scale created a smaller indent, which allowed valid readings in these regions. The results of testing conformed to the governing requirements for each of the parts tested.

Table 3. Hardness testing of body Rockwell "C" scale - 150-kg major load

Reading	HRC
1	38.4
2	39.7
3	38.4
4	38.5
5	38.9
6	39.1
7	40.0
8	38.7
9	36.9
10	37.4
Average	38.6
Drawing Requirement 7-211411186	35 - 42

Table 4. Hardness testing of outer ring Rockwell "15-N" scale - 15-kg major load

Reading	HR15-N	HRC
1	78.1	36.0
2	75.5	31.0
3	76.6	33.0
4	74.8	30.0
5	78.6	37.0
6	77.0	34.0
7	75.1	30.0
8	75.7	31.0
9	75.6	31.0
10	74.6	29.0
Average	76.2	32.0
Drawing Requirement 7-211411186	-	28 - 37

Table 5. Hardness testing of ball Rockwell "15-N" scale - 15-kg major load

Reading	HR15-N	HRC
1	89.7	59.0
2	88.3	56.0
3	89.1	58.0
4	88.9	57.0
5	88.2	56.0
6	89.1	58.0
7	89.7	59.0
8	88.9	57.0
9	89.1	58.0
10	89.0	58.0
Average	89.0	58.0
Drawing Requirement 7-211411186	-	55 min.

8. Micro-Hardness Testing

Micro-hardness profiles were taken on the metallographically polished transverse and longitudinal cross sections of the failed ball. This was performed in order to determine the presence and thickness of any possible surface chemistry gradients. Paragraph 3.3.2.4 of HP1-1 states that the depth of carburization, decarburization, or nitriding shall be determined by a micro-hardness traverse. Carburization and/or nitriding are disallowed per HP1-1. The boundary of the carburization, decarburization, or nitriding shall be at the depth at which the hardness rises/falls to the equivalent of 20 points Knoop above/below the core hardness. The Knoop hardness scale was used for this testing, and the readings were obtained in a staggered traverse to maximize the amount of readings that could be taken close to the surface, while maintaining the rule-of-thumb distance between indents. Four sets of readings were taken on each specimen. Figure 33 illustrates the location of the hardness profiles on the metallographic cross sections.

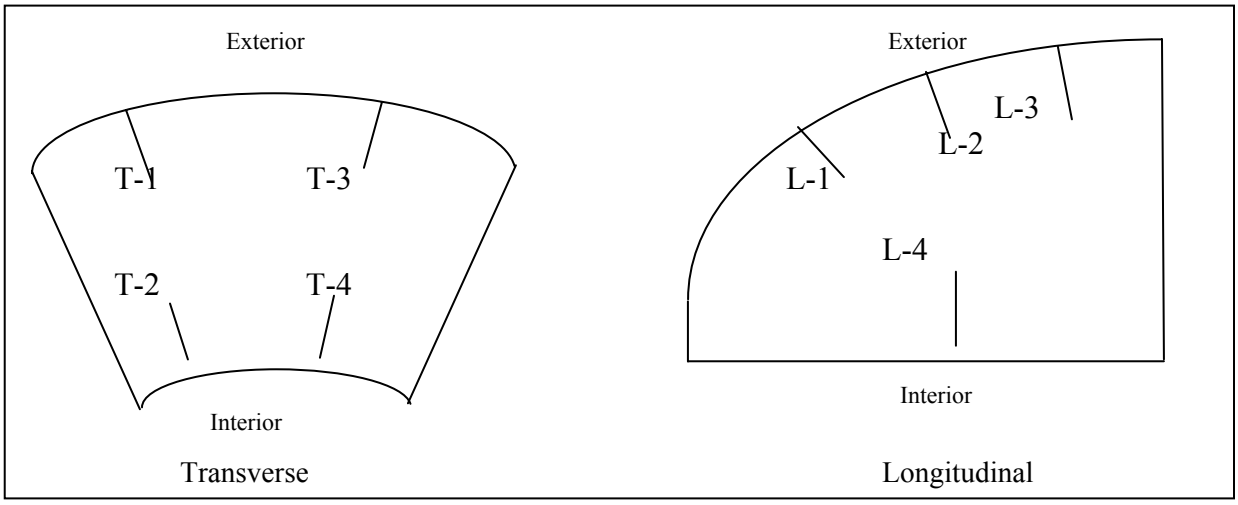

Figure 33. Schematic of hardness profile traverses.

Profiles T-1, T-2, T-3, T-4, L-1, L-3, and L-4 (see tables 6 through 13) were all softer within the first 1 to 3 mils' depth than the core hardness. This depth was within the requirement set forth in Paragraph 2.1.1.2 of HP 1-1, "*Such partial decarburization shall be judged excessive if greater than 0.003 inch deep on any finish-machined surface.*" However, this gradient may have been attributed not only to a difference in surface chemistry but also to the fact that the first reading on each specimen was only 1 mil from the surface. Edge effects may have played a role in the resultant first hardness readings on each profile. Disregarding the first reading, profiles T-1, T-2, T-3, T-4, L-3, and L-4 showed no appreciable gradient. In most cases, each value in a given profile was within 20 to 30 points Knoop, when the first three readings were disregarded.

Table 6. Knoop hardness profile T-1

Depth (mils)	Knoop	Equivalent HRC
1	522.3	48.7
3	682.4	57.6
5	707.1	58.8
7	754.5	61.0
9	745.3	60.6
11	745.3	60.6
12	746.8	60.6

Table 7. Knoop hardness profile T-2

Depth (mils)	Knoop	Equivalent HRC
1	689.2	57.9
2	708.6	58.9
4	720.0	59.4
6	701.5	58.5
8	700.1	58.5
10	689.2	57.9
12	717.1	59.3

Table 8. Knoop hardness profile T-3

Depth (mils)	Knoop	Equivalent HRC
1	653.9	56.1
2	720.0	59.4
3	718.6	59.3
4	705.7	58.7
5	736.2	60.1
6	745.3	60.6
7	730.3	59.9
8	710.0	59.0
9	730.3	59.9
10	720.0	59.4
11	727.3	59.7
12	722.9	59.5

Table 9. Knoop hardness profile T-4

Depth (mils)	Knoop	Equivalent HRC
1	611.0	53.9
2	725.8	59.7
3	710.0	59.0
4	740.7	60.3
5	734.7	60.1
6	748.3	60.7
7	718.6	59.3
8	704.3	58.7
9	715.7	59.2
10	717.1	59.3

Table 10. Knoop hardness profile L-1

Depth (mils)	Knoop	Equivalent HRC
1	573.2	51.8
2	650.2	56.0
3	683.8	57.6
4	705.7	58.7
5	675.8	57.2
6	697.4	58.3
7	712.8	59.1
8	720.0	59.4
9	696.0	58.3
10	693.2	58.1
11	694.6	58.2
12	717.1	59.3
13	707.1	58.8
14	704.3	58.7
15	704.3	58.7

Table 11. Knoop hardness profile L-2

Depth (mils)	Knoop	Equivalent HRC
1	512.6	48.1
2	607.6	53.7
3	601.0	53.3
4	603.2	53.5
5	604.3	53.5
6	615.6	54.2
7	609.9	53.8
8	626.0	54.7
9	628.4	54.9
10	655.2	56.2
11	644.0	55.7
12	655.2	56.2
13	653.9	56.1
14	666.7	56.8
15	653.9	56.1
16	664.1	56.7
17	681.1	57.5
18	704.3	58.7
19	682.4	57.6
20	707.1	58.8
21	696.0	58.3
22	722.9	59.5
23	711.4	59.0
24	714.2	59.1
25	705.7	58.7
26	698.8	58.4
27	711.4	59.0
28	714.2	59.1
29	712.8	59.1
30	724.4	59.6
31	722.9	59.5
32	725.8	59.7
33	698.8	58.4
34	694.6	58.2
35	704.3	58.7
36	683.8	57.6

Table 12. Knoop hardness profile L-3

Depth (mils)	Knoop	Equivalent HRC
1	441.7	43.2
2	673.2	57.1
3	671.9	57.0
4	679.8	57.4
5	679.8	57.4
6	691.9	58.0
7	704.3	58.7
8	701.5	58.5
9	693.2	58.1
10	693.2	58.1
11	693.2	58.1
12	707.1	58.8
13	702.9	58.6
14	687.8	57.8
15	693.2	58.1

Table 13. Knoop hardness profile L-4

Depth (mils)	Knoop	Equivalent HRC
1	687.8	57.8
2	705.7	58.7
3	710.0	59.0
4	746.8	60.6
5	746.8	60.6
6	742.2	60.4
7	746.8	60.6
8	742.2	60.4
9	742.2	60.4
10	742.2	60.4

Profile L-2 (see figure 39) exhibited different characteristics, which was the reason a greater number of readings was taken (36). The first 16 readings (representing a total of 16 mils in depth) were lower in hardness by at least 20 points Knoop than the remaining values. This would have suggested a depth of decarburization (or other surface chemistry difference) of 16 mils. However, considering that adjacent profiles to the left (L-1, figure 38) and right (L-3, figure 40) of profile L-2 did not exhibit this feature, and the fact that the region appeared similar to L-1 and L-3 metallographically, ARL felt that there was no reason for concern.

9. Scanning Electron Microscopy and Energy Dispersive Spectroscopy

One half of the sectioned component was thoroughly cleaned and prepared for examination. The fracture half of the ball was examined with a Japan Electron Optics Laboratory JSM[4]-840A scanning electron microscope (SEM) and a Kevex SIGMA series energy dispersive spectroscopy (EDS) system. The failure origin (indicated by the white arrow) and surrounding area can be observed in figure 34.

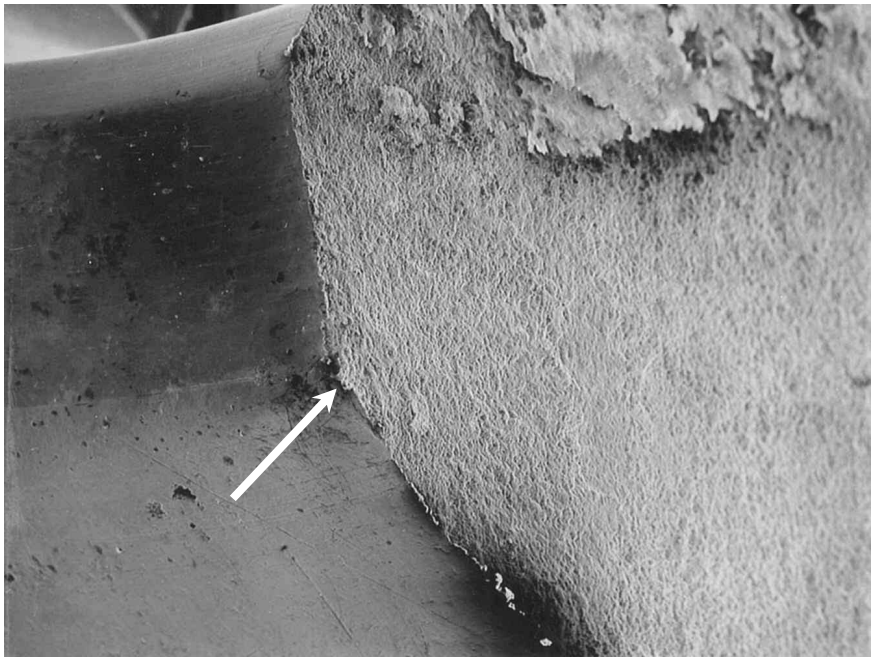

Figure 34. Failure origin area of the 440C ball (mag. 30x).

Closer inspection revealed inter-granular attack within and near the origin. Figure 35 depicts the likely fracture origin and the surrounding area at higher magnification at a 45-degree tilt angle with respect to the fracture surface. The large area of attack near the origin in figure 35 can be observed in figure 36.

[4]JE06 series model

Figure 35. Fracture origin at high magnification and 45° tilt (mag. 250x).

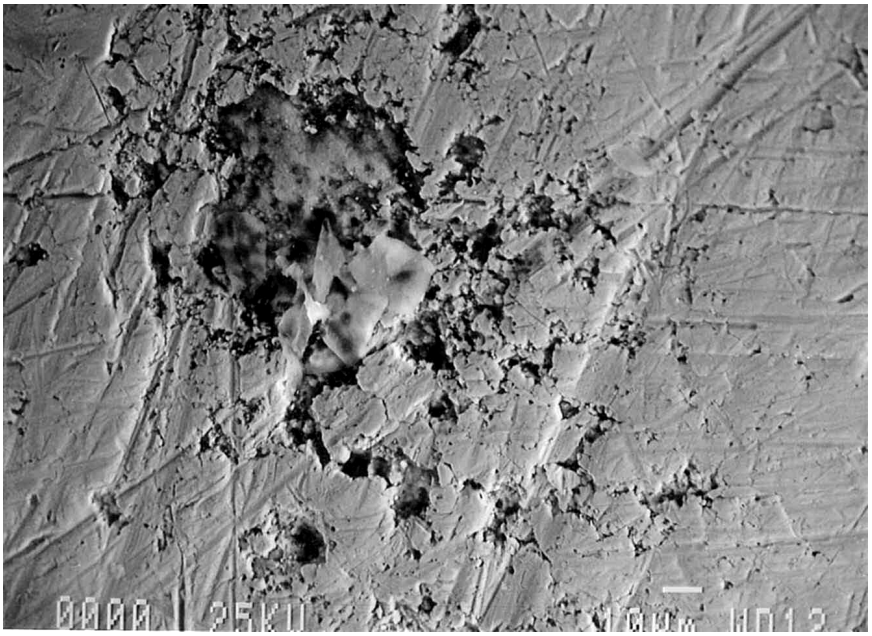

Figure 36. Area of inter-granular attack near the origin (mag. 500x).

The attacked area was filled with corrosion product. This product was analyzed with EDS. The EDS spectrum produced from this product can be observed in figure 37. It was similar in chemistry and composition to the other attacked areas on the ball. However, it was slightly different from the corrosion product on the fracture surface that is presented later.

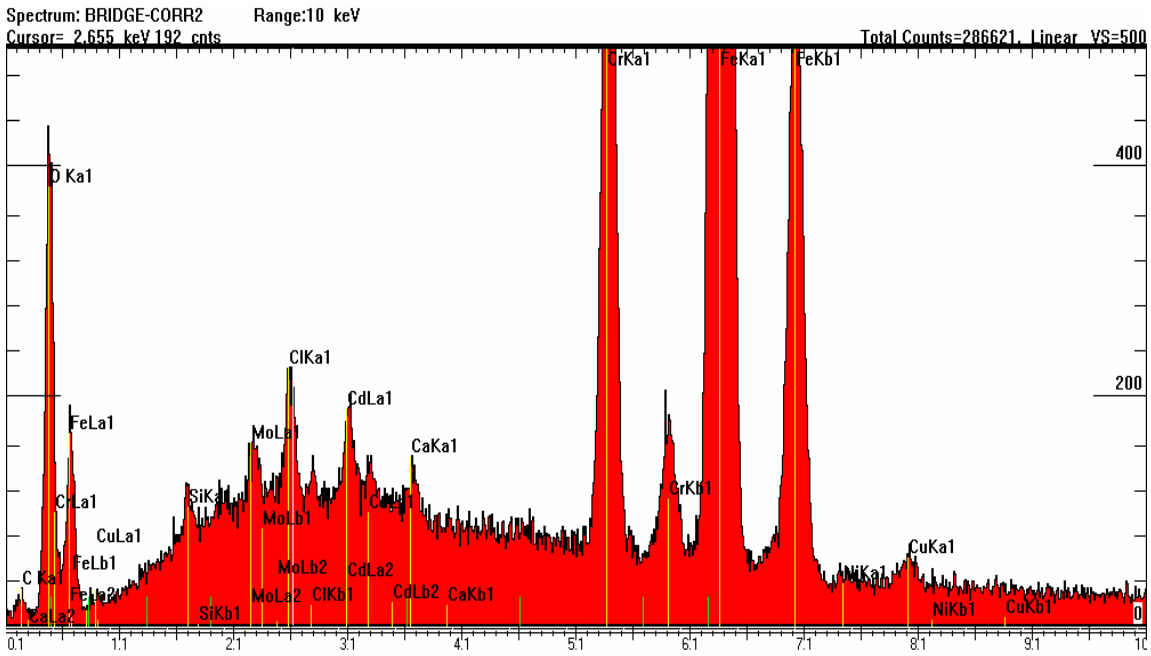

Figure 37. EDS spectrum collected from the product within the inter-granular attack.

The corresponding quantitative analysis of this product is presented in table 14. This spectrum, along with the other EDS data presented, can be contrasted with the base material spectrum that is presented in figure 38 along with its corresponding qualitative and quantitative analysis in table 15.

Table 14. Qualitative and quantitative analysis of the corrosion product within the inter-granular attack

Element	Line	Weight Percent	Error	K-Ratio	Counts per Second	Atomic Percent
C	Ka	8.70	0.452	0.0170	1.85	25.67
O	Ka	10.47	0.127	0.0295	34.23	23.18
Si	Ka	1.29	0.022	0.0062	16.99	1.63
Cl	Ka	1.80	0.022	0.0137	33.51	1.80
Ca	Ka	1.22	0.018	0.0116	23.49	1.08
Cr	Ka	7.73	0.050	0.0828	118.17	5.27
Fe	Ka	58.21	0.166	0.5424	617.04	36.93
Ni	Ka	1.44	0.031	0.0123	10.78	0.87
Cu	Ka	2.23	0.042	0.0185	14.12	1.24
Mo	La	2.90	0.044	0.0214	21.32	1.07
Cd	La	4.02	0.050	0.0341	32.37	1.27

Naturally occurring chloride salts can explain the presence of calcium and chlorine. The copper, nickel, and molybdenum are alloying elements within the material, so it is understandable that they are revealed within the corrosion product. The cadmium, however, must have originated from a foreign source to this ball. This is discussed in more depth later.

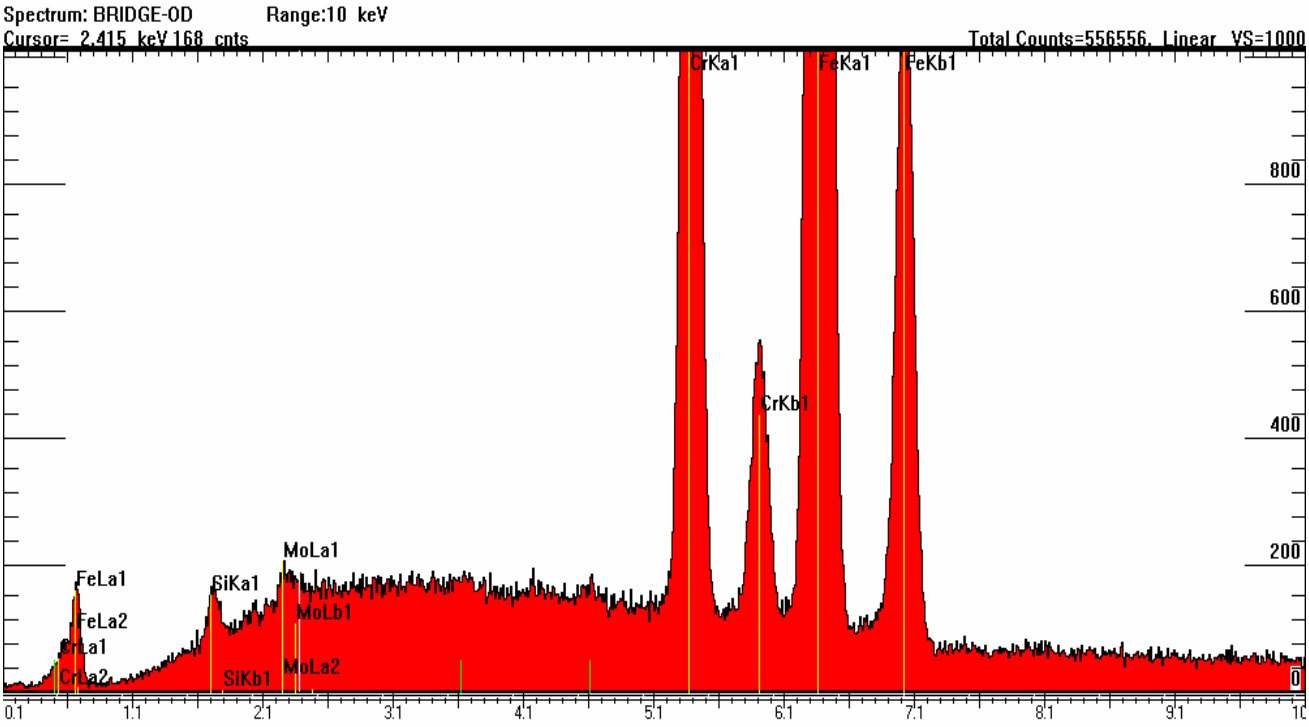

Figure 38. EDS spectrum collected from the base material of the failed component.

Table 15. Qualitative and quantitative analysis of the base material of the failed component

Element	Line	Weight Percent	Error	K-Ratio	Counts per Second	Atomic Percent
Si	Ka	1.07	0.017	0.0047	19.21	2.10
Cr	Ka	18.29	0.061	0.2138	451.55	19.36
Fe	Ka	78.34	0.156	0.7459	1256.10	77.22
Mo	La	2.30	0.033	0.0164	24.21	1.32

The inter-granular attack at the origin was neither the only nor the largest site of its kind on the ball. Several localized inter-granular attacked sites existed along the exterior surface. Overall, it was estimated that less than 5% of the exterior surface contained corrosion. The hole bored through the ball, however, was noticeably void of inter-granular attack. This would provide evidence that either the attack took place before the hole was made or the hole was somehow shielded from the attack. It is suspected that the combination of the inter-granular attack occurring at a concentrated stress site, the edge of the component, was likely the cause of failure even though much larger attacked areas existed. Two relatively large areas of the attack are observable in figure 35. These areas are depicted at higher magnification in figure 39. The corrosion sites measured approximately 0.0015 inch deep.

Both sites contained some corrosion product, and a noticeable distinction was discernible. The inter-granular attack was preferential to the precipitates at or near the grain boundaries. Closer examination of the region on the left in figure 39 revealed that the precipitates themselves are not

attacked. Conversely, they are dislodged by the attack. Figure 40 depicts this region. The depletion of chromium in the regions surrounding the precipitates makes this occurrence intuitive. The white arrows indicate the precipitates in advancing stages of dislodgment. Figure 41 presents the precipitates shown in figure 40 at higher magnification. Other inter-granular attacked areas demonstrated evidence leading to this conclusion.

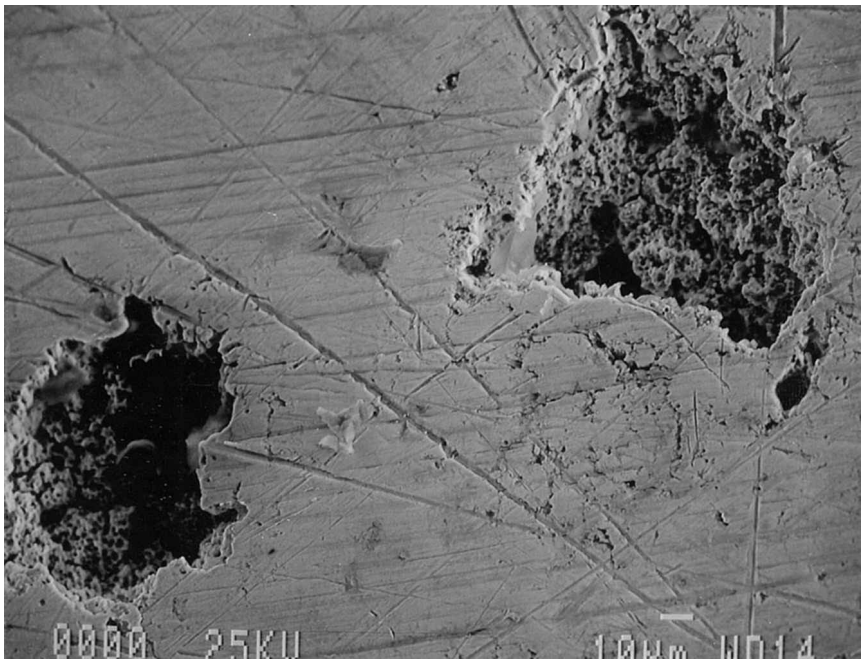

Figure 39. Two large areas of inter-granular attack near the origin (mag. 400x).

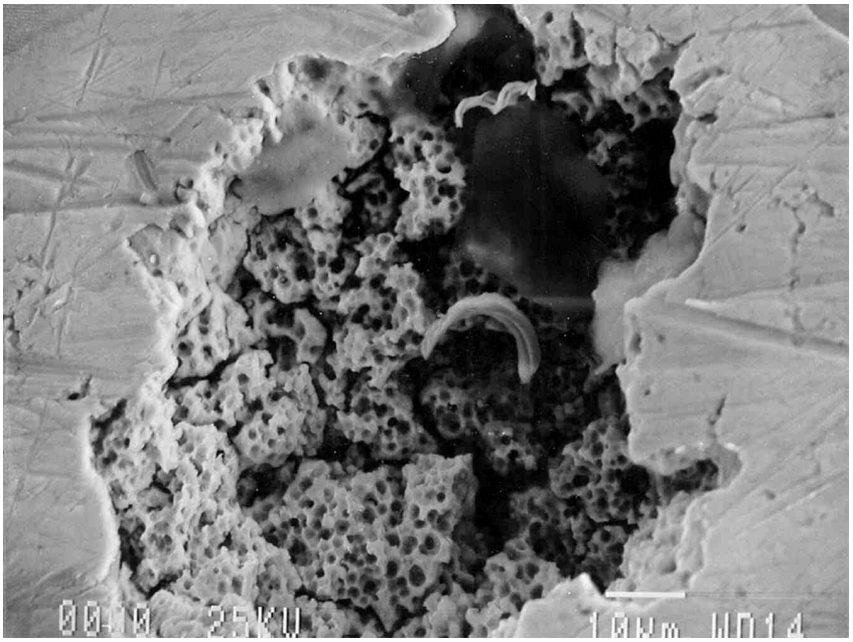

Figure 40. Inter-granular attack site with dislodged precipitate (mag. 1kx).

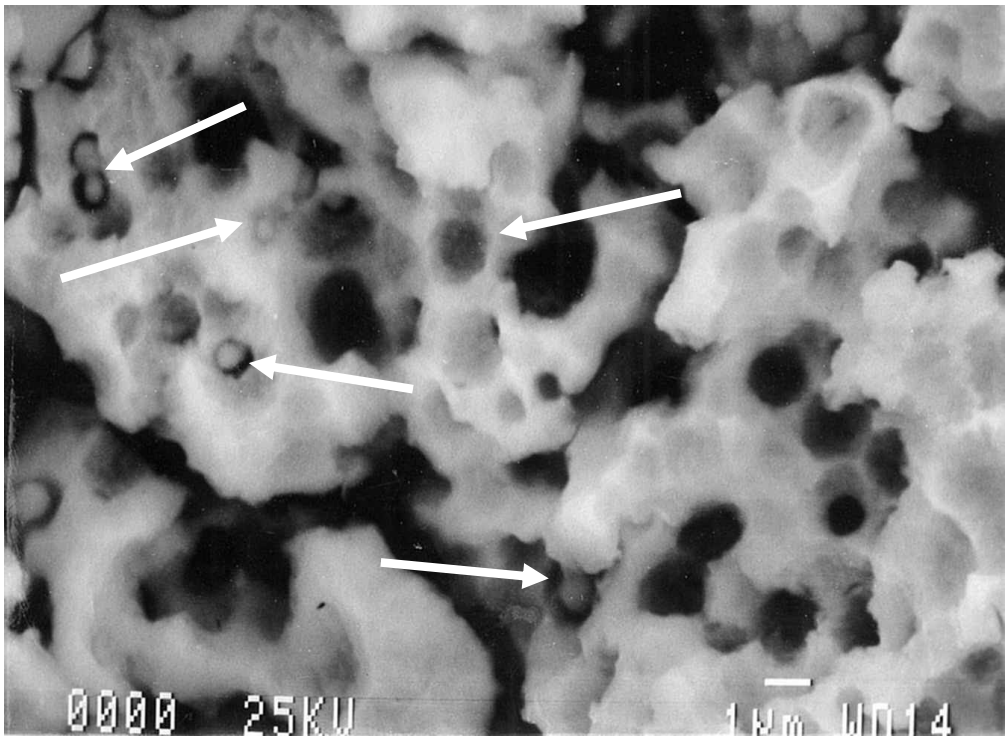

Figure 41. High magnification showing detail of figure 40 (mag. 5kx).

Figure 42 was situated approximately 1 mm from the origin along the fracture surface. Inter-granular attack around precipitates near the surface is indicated by the arrows. Another region adjacent to the fracture surface, figure 43, depicts attack around precipitates as well as dislodged precipitates embedded within the corrosion product on the fracture surface. High magnification of another attacked area away from the fracture surface shows four distinct precipitates clearly dislodged from the matrix material. These precipitates are shown in figure 44. The EDS spectrum of the precipitates displayed increased levels of chromium and carbon compared with the matrix base material as might be expected with the formation of iron-chromium carbides of this material (see Metallography section). Figure 45 displays this spectrum and the corresponding increases in chromium and carbon compared with the base material. Note that no carbon was detectable by EDS within the base material. Table 16 shows the qualitative and quantitative results generated from the spectrum.

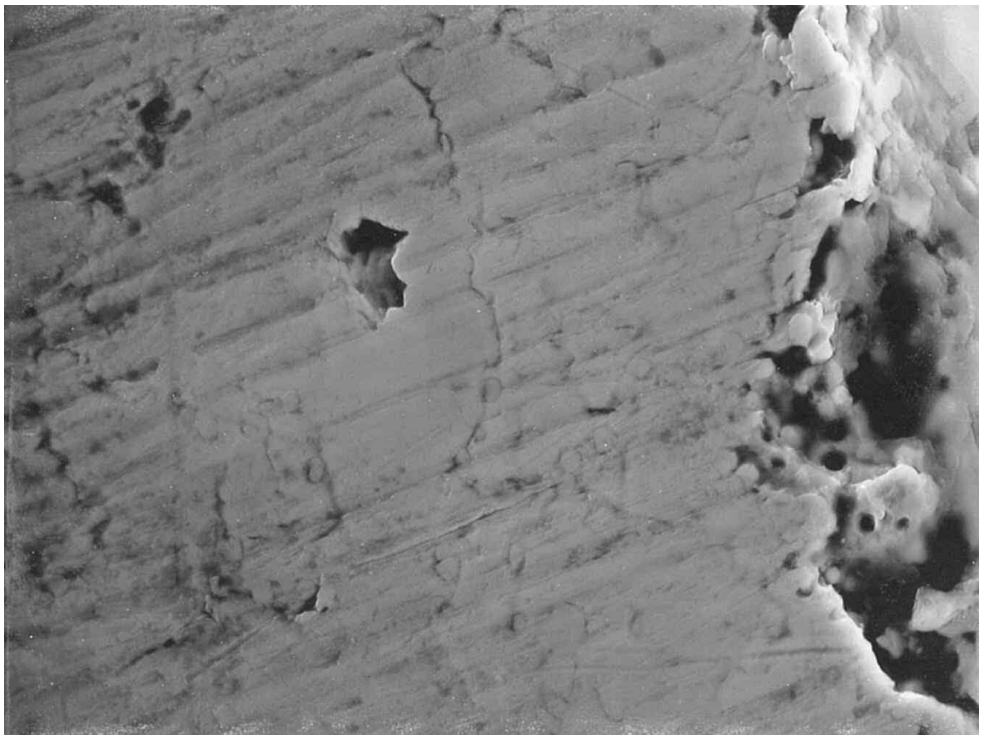

Figure 42. Inter-granular attack preferentially around precipitates (mag. 2kx).

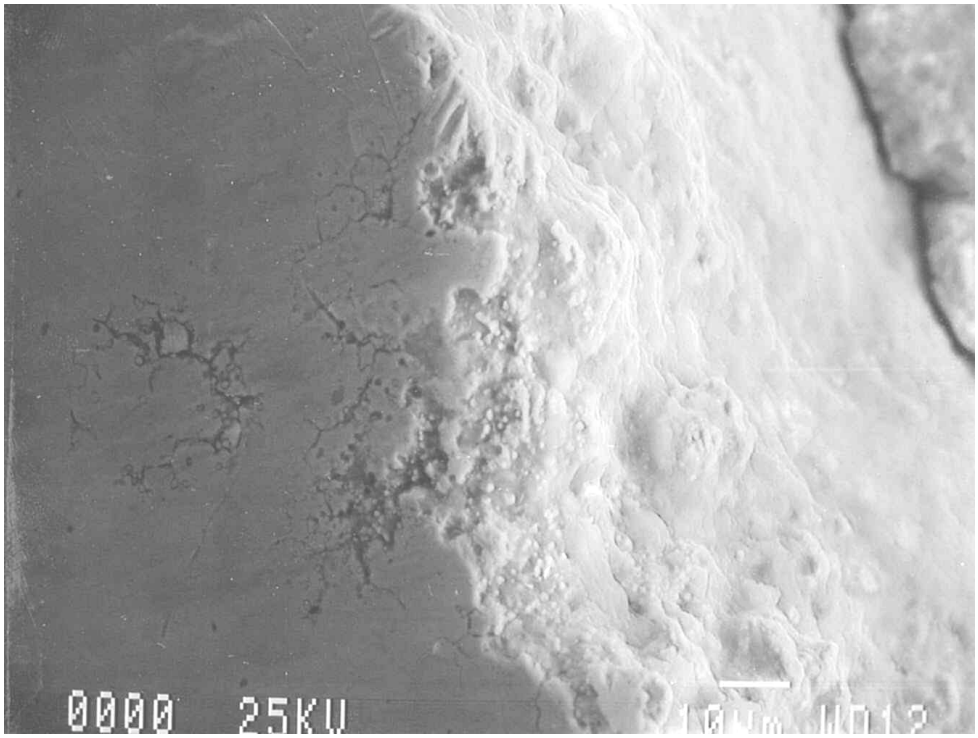

Figure 43. Attack around precipitates and dislodged precipitates (mag. 750x).

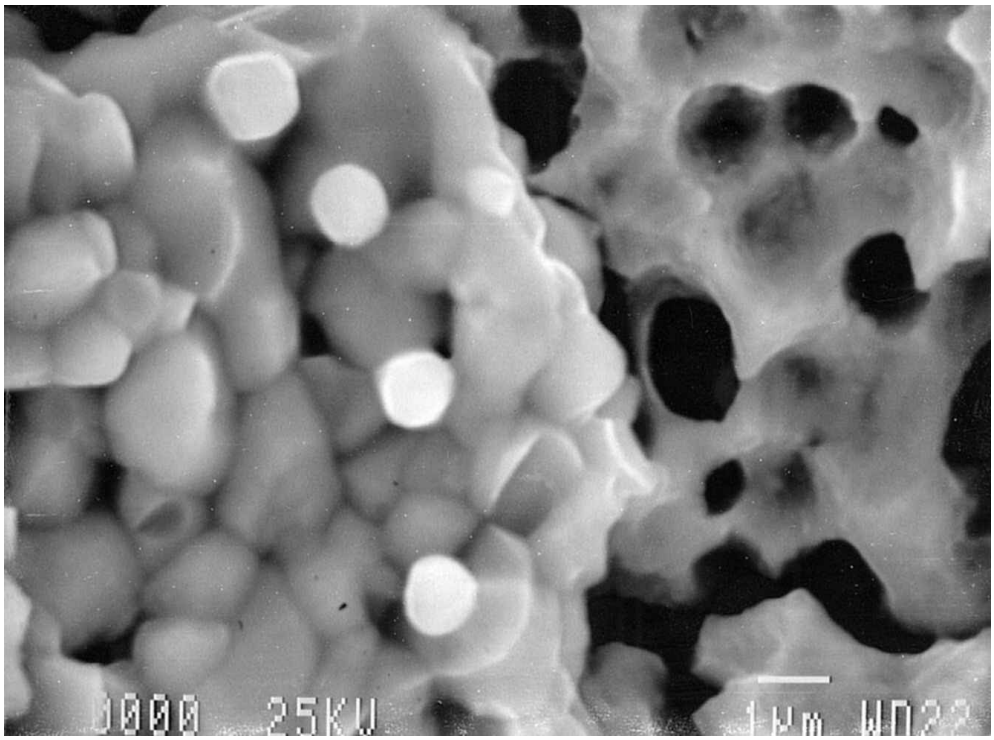

Figure 44. Four distinct dislodged precipitates (mag. 7500x).

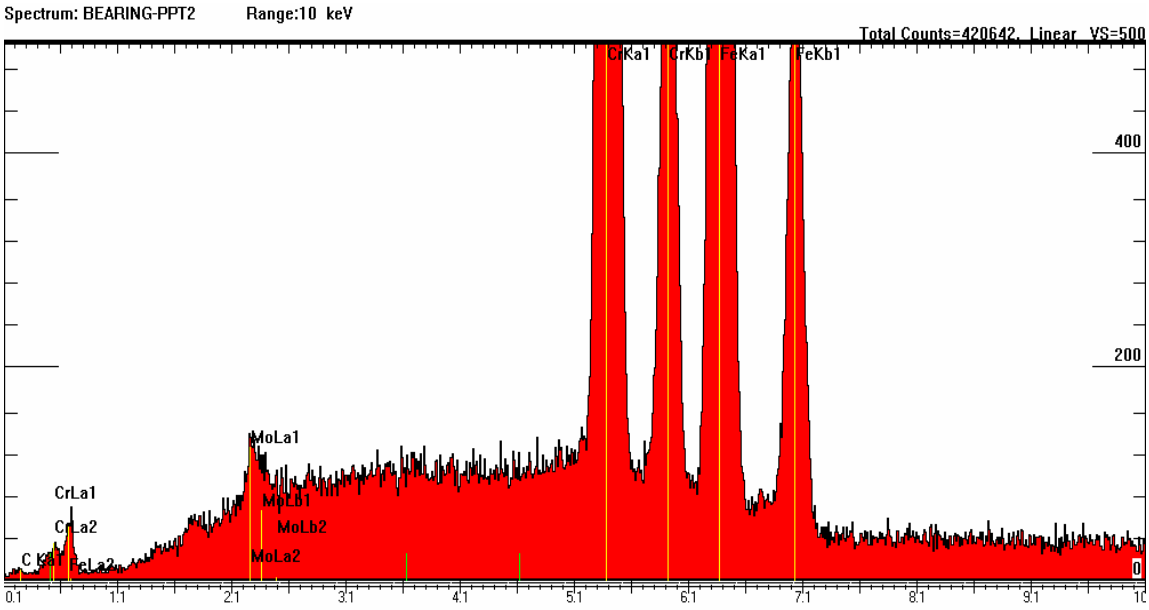

Figure 45. EDS spectrum of the precipitates within the matrix.

Table 16. The qualitative and quantitative analysis of the precipitates

Element	Line	Weight Percent	Error	K-Ratio	Counts per Second	Atomic Percent
C	Ka	2.46	0.274	0.0040	0.25	9.06
Cr	Ka	45.70	0.162	0.4910	395.57	44.38
Fe	Ka	51.05	0.212	0.4530	291.02	46.15
Mo	La	0.79	0.031	0.0059	3.31	0.42

Secondary inter-granular cracks that propagated parallel to the fracture plane were observed within 2 mm of the fracture. These cracks were observed along the flat surface adjacent to the bored hole. Figure 46 depicts the multitude of these cracks highlighted with arrows. At higher magnification (see figure 47), an excellent example of inter-granular cracking preferentially around surface precipitates was observed.

Figure 46. Secondary cracks near and parallel to the fracture surface (mag. 150x).

The fracture surface did not add considerable significant information to that which was concluded from the surface of the ball. Five fractographs were taken evenly spaced across the fracture surface to identify differences as the fracture progressed. The fracture mode, however, was mixed transgranular favored by fatigue and inter-granular favored by corrosion. These fractographs are presented in figures 48 through 52, from the origin. Within these fractographs, it is discernible that the fracture progressed in a mixed mode (trans-granular/inter-granular), aided by alternating stresses and corrosive action. The preferential cracking around the precipitates is readily discernible since several precipitates and cavities are easily recognized. The severity of the corrosion increased with age, toward the origin, as would be expected. The fracture was notably

free of discernible striations. However, typical beach marks were noticed optically and confirmed with the SEM.

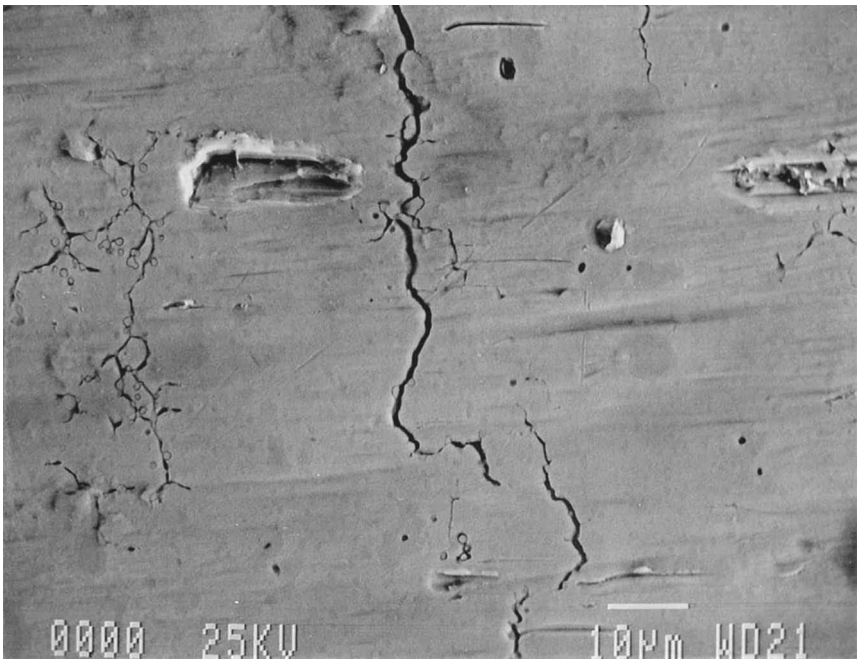

Figure 47. Preferential inter-granular cracking around precipitates (mag. 1kx).

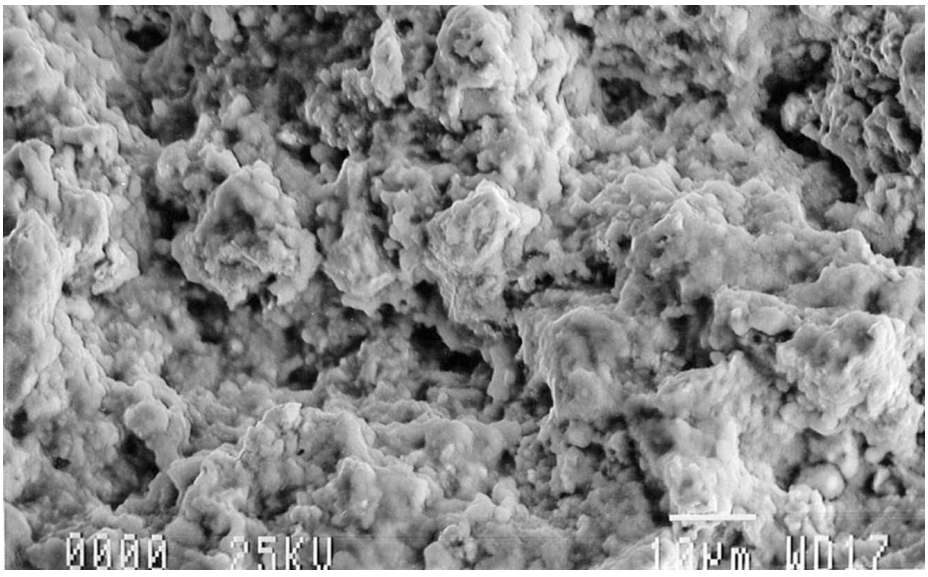

Figure 48. Fractograph 1 of 5, nearest the origin (mag. 1kx).

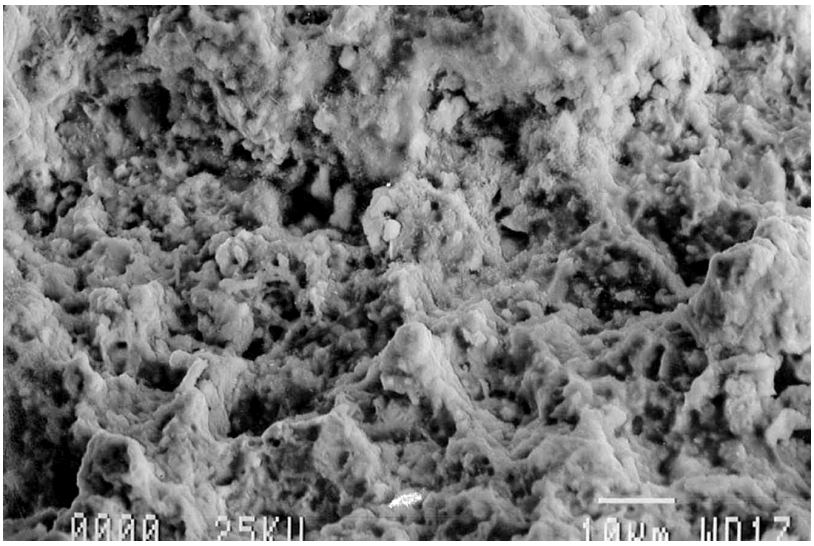

Figure 49. Fractograph 2 of 5, heavily corroded (mag. 1kx).

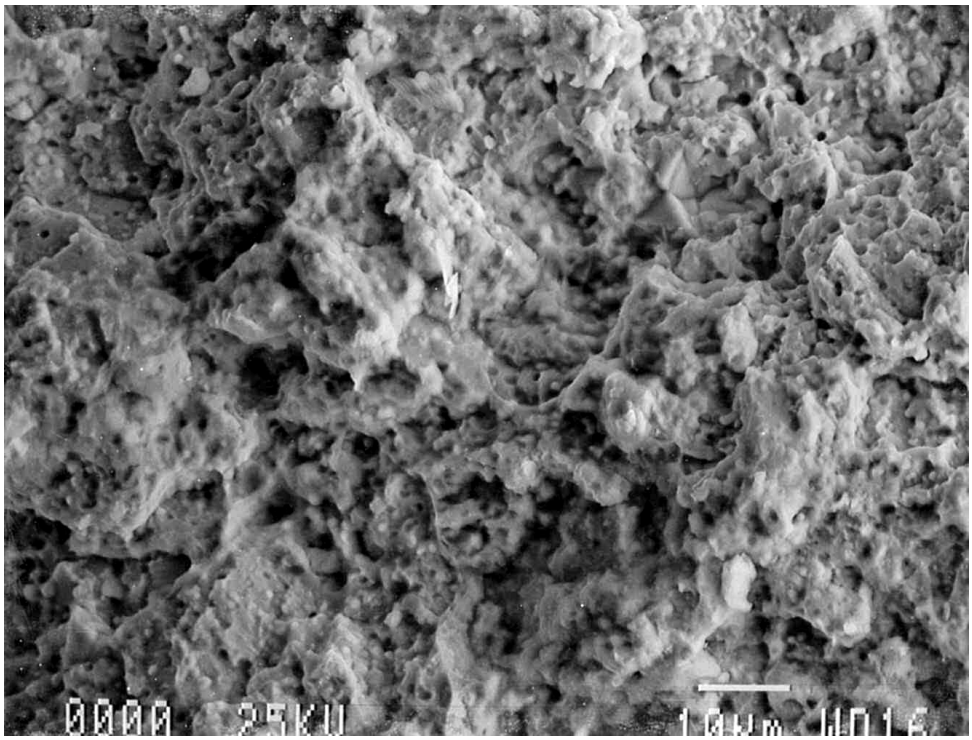

Figure 50. Fractograph 3 of 5, at the midpoint of fracture (mag. 1kx).

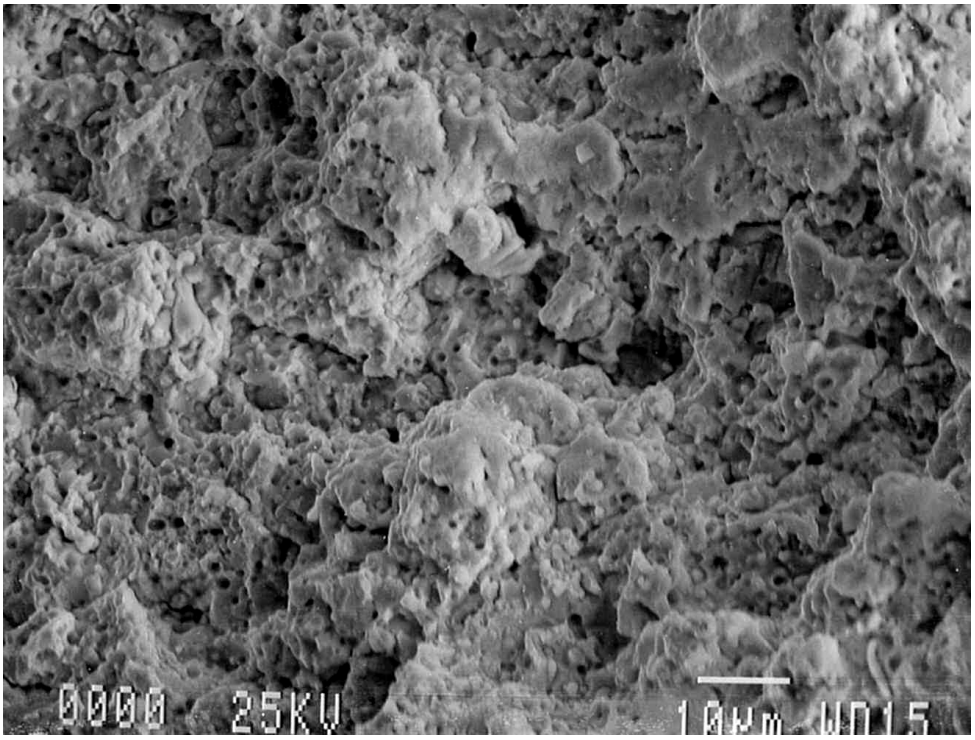

Figure 51. Fractograph 4 of 5, showing only light corrosion (mag. 1kx).

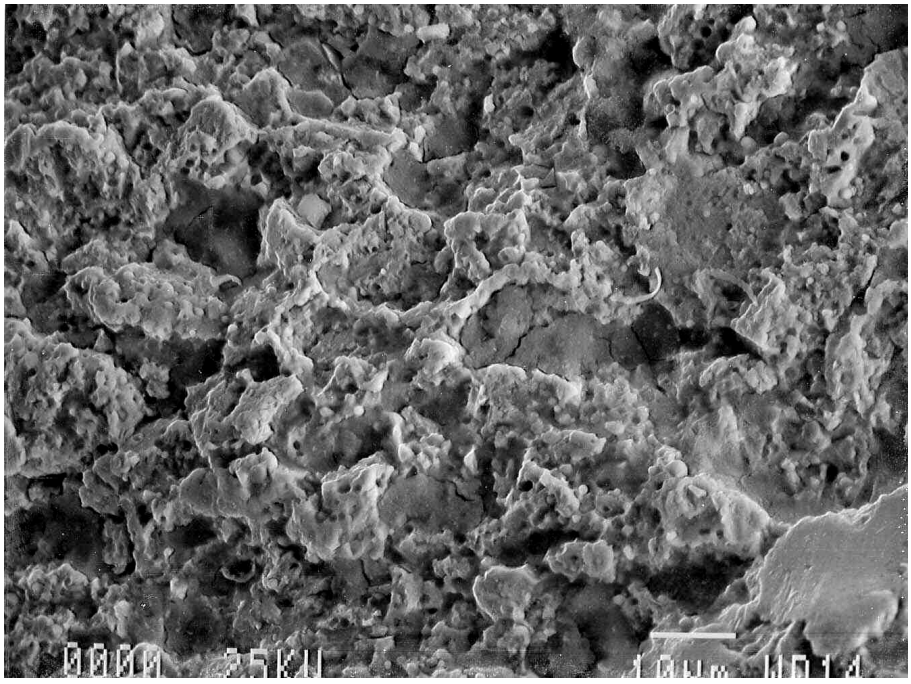

Figure 52. Fractograph 5 of 5, farthest from the origin (mag. 1kx).

The corrosion observed coupled with the fact that noticeable fatigue beach marks were discernible, would lend evidence to corrosion fatigue being the failure mechanism. EDS analysis of the corrosion products on the surface proved slightly different from the corrosion products observed on the surface of the ball. Figure 53 presents the EDS spectrum of the corrosion products on the fracture surface. Table 17 presents the chemical analysis data acquired from that EDS spectrum.

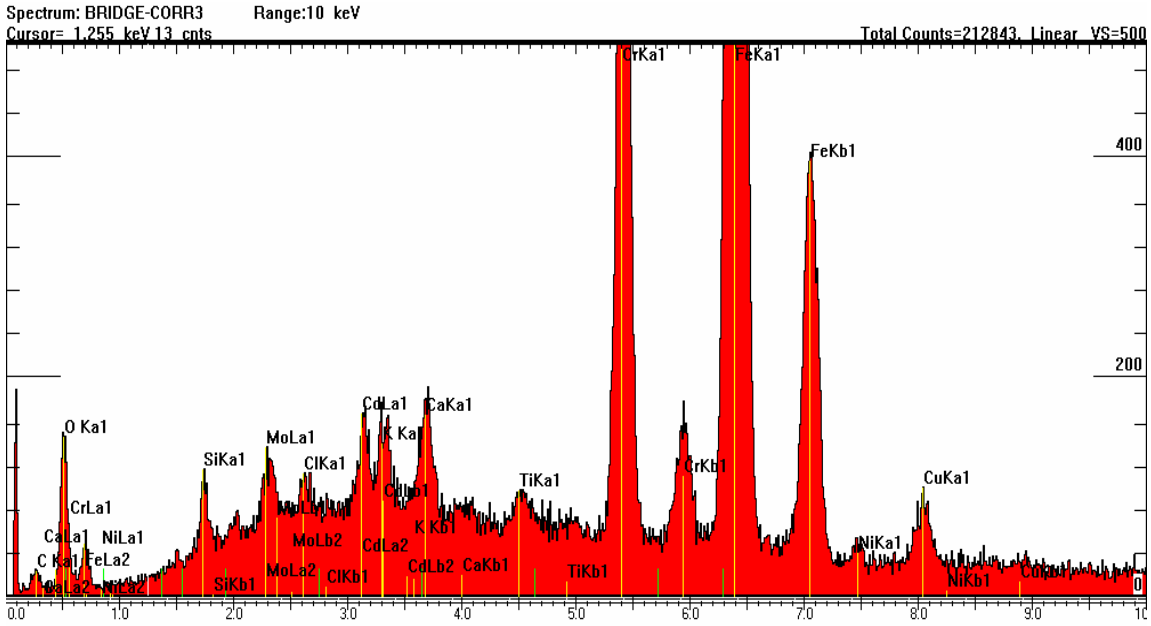

Figure 53. EDS spectrum of the corrosion product on the fracture surface.

Table 17. Qualitative and quantitative analysis of the corrosion product on the fracture surface

Element	Line	Weight Percent	Error	K-Ratio	Counts per Second	Atomic Percent
C	Ka	8.71	0.525	0.0174	1.37	27.99
O	Ka	5.07	0.111	0.0125	10.48	12.24
Si	Ka	1.41	0.027	0.0067	13.40	1.93
Cl	Ka	1.24	0.021	0.0094	16.77	1.35
K	Ka	0.27	0.010	0.0024	3.78	0.26
Ca	Ka	2.39	0.029	0.0229	33.64	2.30
Ti	Ka	1.97	0.029	0.0190	23.77	1.59
Cr	Ka	11.40	0.073	0.1189	122.89	8.46
Fe	Ka	55.22	0.190	0.5121	421.99	38.16
Ni	Ka	1.57	0.038	0.0135	8.55	1.03
Cu	Ka	3.06	0.057	0.0257	14.17	1.86
Mo	La	3.15	0.054	0.0233	16.83	1.27
Cd	La	4.55	0.062	0.0390	26.80	1.56

The additional elements of chlorine, potassium, and calcium can again be explained from typical chloride salts that are naturally occurring. Copper, nickel, and molybdenum were within the matrix, so it is reasonable that the corrosion product could contain these elements. However, titanium and cadmium are not alloying elements of this material, and their existence suggests

that perhaps the mating components could be made of these materials or could contain these elements as typical alloying constituents.

Noticeable burnishing of the ball exterior was evident. The burnishing was attributed to rubbing of the ball with the Teflon-coated outer ring of the component. Approximately 3/4 of the surface of the ball had burnishing in a circumferential pattern where it mated with the outer ring. Although this burnishing obscured the inter-granular attack on the exterior surface of the ball, it was still discernible. The attack appeared uniform and was not influenced by the outer ring.

10. Retained Austenite

The specimens used for metallographic examination were subjected to retained austenite measurement via x-ray diffraction. Governing specification HP 1-1 does not list a requirement with respect to retained austenite, but Mr. John Magee from Carpenter Specialty Alloys indicated that a value of 10% should not be exceeded (*1*). The requirements of HP 1-1 (subzero cooling to about –100° F, followed by double tempering), if performed properly, should yield an acceptable level of retained austenite.

The retained austenite was measured with a Technology for Energy Corporation (TEC) x-ray stress analysis system. The retained austenite analysis software incorporated by the TEC system compares the measured integrated intensity of the diffraction peaks from the martensite/ferrite alpha phase and austenite gamma phases with calculated theoretical intensities. The software is based on the requirements of ASTM-E-975 (*2*). Quantification of the martensite/ferrite and austenite volume fractions is possible because the total integrated intensity of the diffraction peaks for each phase is proportional to the volume fraction of that phase. Since other phases (such as carbides) may generate diffraction peaks of sufficient intensity and at angular positions so as to interfere with the martensite/ferrite and/or austenite peaks (and subsequently resulting in a biased retained austenite measurement), the volume fraction of carbides was determined. Type 440C steel nominally contains approximately 12% carbides. The TEC software requires a percent volume of carbides in the sample as part of the analytical input, and as such, both 10% and 20% carbide content were used, representing a boundary by which to quantify the retained austenite.

Readings were taken directly on the metallographic samples, which were polished to the 0.05-micron alumina level. The readings were similar in magnitude and less than the "10% maximum" criterion, as listed in table 18.

As could be expected, the percent retained austenite (%RA) values at the 20% carbide level were slightly lower than at the 10% carbide level. It was also noted that the transverse section contained more %RA than the longitudinal sample. Each reading was below the "10% maximum" requirement.

Table 18. Retained austenite measurements - 0.05-micron alumina polish

Sample	Percent Retained Austenite Assuming 10% Carbides	Percent Retained Austenite Assuming 20% Carbides
Longitudinal	5.8%	5.2%
Transverse	7.5%	6.7%

In order to ensure that the grinding and polishing process did not transform any austenite into martensite, the specimens were removed from the mounting material and electropolished, and approximately 5 mils were removed from the polished surfaces. Again, the results were less than the "10% maximum" criterion, as presented in table 19, and were generally the same magnitude as the readings obtained on the alumina polished samples. The readings on the transverse sample were higher than those from the longitudinal sample, similar to the alumina polished samples.

Table 19. Retained austenite measurements – electro-polished surface

Sample	Percent Retained Austenite Assuming 10% Carbides	Percent Retained Austenite Assuming 20% Carbides
Longitudinal	4.9%	4.4%
Transverse	7.0%	6.2%

11. Sensitization Testing

It was speculated that this component was perhaps sensitized during production because of the presence of inter-granular attack at the surface. Specification HP 1-1 summarizes a laboratory test that was used by ARL to determine whether the component had been sensitized. Paragraph 3.3.2.5 states that type B steels (type 440C) shall be metallographically prepared and etched for 1 to 2 minutes in a freshly prepared solution consisting of 1 gram of picric acid, 5 ml of hydrochloric acid, and 100 ml ethanol. Paragraph 2.1.1.4 indicates that components with ultimate tensile strength greater than 220 ksi shall not exhibit inter-granular attack greater than 0.0005 inch in depth. The sample showed negligible evidence of inter-granular attack as a result of this test (see figure 54), which did not exceed the depth requirement. In addition to the metallographic sample, ARL subjected a piece of the actual component in the as-received condition to the etchant. Photographs were taken before and after the application of the etchant (figures 55 through 58, respectively) on both the as-received surface and a machine cut surface. There was no evidence of inter-granular attack on any of these surfaces.

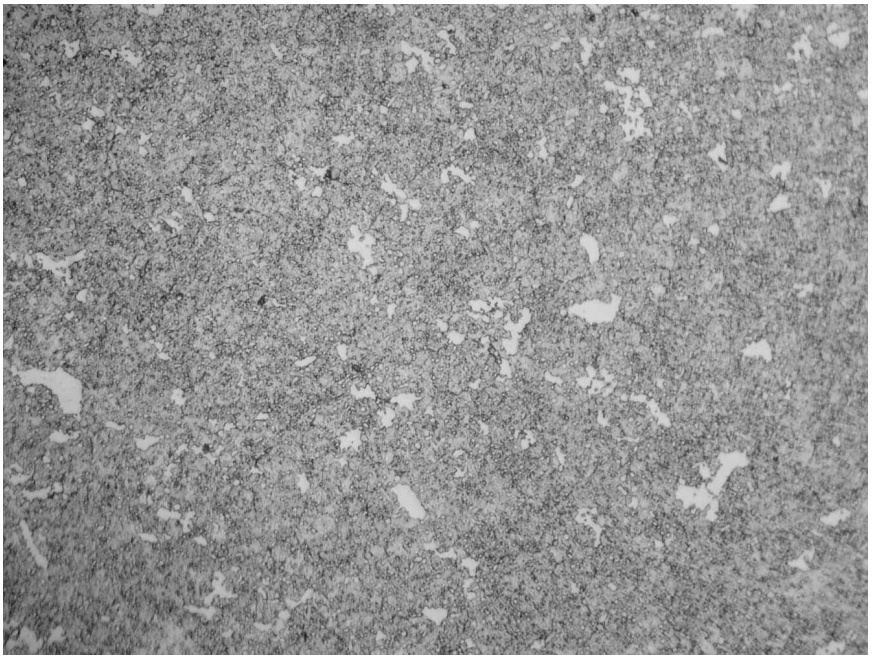

Figure 54. Structure of type 440C steel after sensitization testing (negligible inter-granular attack was noted as a result of this testing) (mag. 400x).

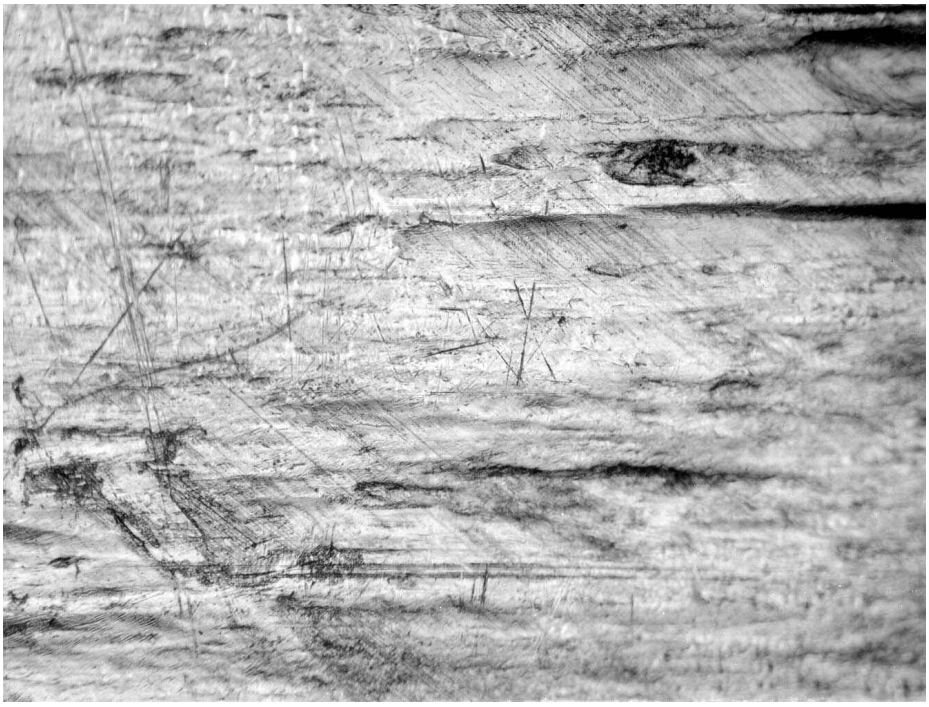

Figure 55. Macrograph of as-received surface of rod end fitting ball (mag. 100x).

Figure 56. Macrograph of as-received surface of rod end fitting ball subjected to sensitization testing (no inter-granular attack was noted) (mag. 100x).

Figure 57. Macrograph of machined surface of rod end fitting ball (mag. 100x).

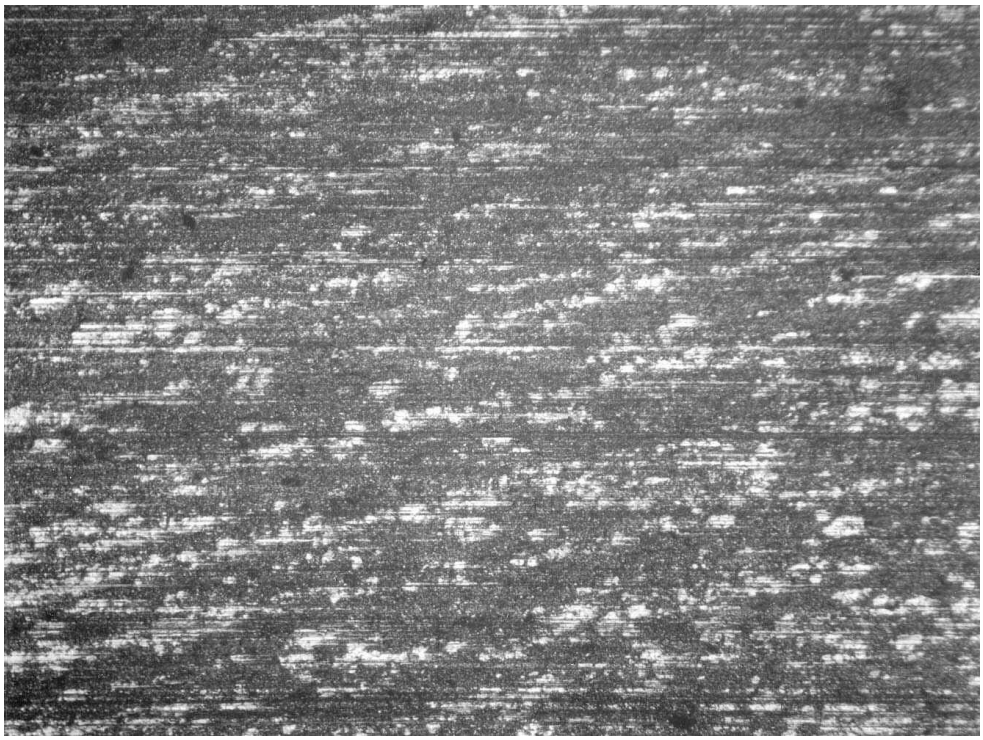

Figure 58. Macrograph of the machined surface of rod end fitting ball subjected to sensitization testing (no inter-granular attack was noted (mag. 100x).

12. Discussion

12.1 Corrosion Fatigue

Corrosion fatigue is a failure mechanism that combines a corrosive environment with an alternating stress field, causing fatigue crack initiation and propagation (*2*). In most cases, the presence of just one of these conditions is not enough to cause component failure. Based on the regions of corrosive attack noted along the periphery of the ball and the evidence of beach marks on the cleaned fracture surface, it was concluded that this was the most likely failure mechanism for the part undergoing investigation.

12.2 Quench Cracking

The dimensions of components change as a result of the heating and quenching process. The dimensions change because of the volume expansion occurring as one phase transforms into another phase (i.e., austenite to martensite) or simply, the same phase may change because of the temperature extremes. Stresses formed by the transformation of austenite to martensite (as pertaining to type 440C) are the most critical (*3*). In some cases, these stresses are high enough

to cause cracks upon quenching. High carbon and tool steels, which exhibit high hardness, are most notably susceptible to quench cracking. Another contributory factor is the presence of stress concentration points, such as sharp corners or deep stampings. The fracture paths of the quench cracks are consistently inter-granular, as the path tends to follow the prior austenitic grains. Given the fact that the fracture surface exhibited mixed mode trans-granular/inter-granular morphology, given the corrosive action observed and the fact that the geometry of the ball is not conducive to areas of stress concentration, quench cracking was eliminated as the failure mechanism for the part undergoing investigation.

12.3 Temper Embrittlement

The Alloy Digest (*4*) states that for a combination of maximum hardness and toughness, type 440C stainless steel should be tempered at 800° F. It also mentions to avoid tempering between 800° F and 1050° F, particularly if the part is subject to impact loads, and if hardness and other properties are to be closely controlled. Further, it states that the alloy is subject to temper embrittlement when slowly cooled from this range. Table III of Specification HP 1-1 lists a temper temperature of 450° F for HRC 55 minimum, which indicates that unless the temperature of the tempering furnace was out of control by ~100%, temper embrittlement could not have occurred. Proof of previous thermal treatment at an excessive temperature may be evidenced by cracked carbides within the martensitic matrix (*1*). There was no evidence of cracked carbides upon an examination of the longitudinal or the transverse metallographic sections. Additionally, similar to quench cracking, this failure mechanism always produces an inter-granular fracture path. As previously mentioned, the fracture surface of the part undergoing investigation was mixed mode trans-granular/inter-granular, which eliminated this fracture mechanism.

12.4 Type 440C Stainless Steel

American Iron and Steel Institute type 440C stainless steel is a general purpose hardenable stainless steel, which develops maximum hardness with high strength and corrosion resistance upon quenching (*5*). The wear resistance is derived not only from the heat treatment but also from the chemical composition. The corrosion resistance of this steel is maximized when surfaces are polished to a high luster. However, the corrosion resistance of this alloy does not compare favorably to other types of stainless steels, as shown in table 15 (*6*). It is assumed that this table is for type 440C in the hardened and tempered condition, and not as annealed. Nevertheless, the choice of type 440C becomes evident when one is analyzing the data in table 16 (*7*). As listed, type 440C hardened to 56 HRC exhibited the lowest volume loss when tested for adhesive wear at 10,000 and 40,000 cycles. No other stainless steel at a similar hardness level (S42010, type 420 and S13800) achieved similar wear properties. In the selection of this alloy, some corrosion resistance is sacrificed for exceptional wear characteristics.

12.5 Sensitization

Evidence of inter-granular corrosion of a stainless steel is generally the result of sensitization. This condition occurs when a thermal cycle leads to grain boundary precipitation of carbides, nitrides, or other inter-metallic phases without providing sufficient time for chromium diffusion to fill the locally depleted region (*8*). Sensitization usually becomes a factor when the part is subjected to a corrosive environment and can also lead to such problems as pitting, crevice corrosion, and stress corrosion cracking. However, when sections of the failed component were subjected to the sensitization test outlined in Specification HP 1-1, there was negligible evidence of inter-granular attack. Based on the results of this testing, it was concluded that the part was not sensitized.

13. Failure Scenario

Inter-granular corrosive attack of the ball produced local stress concentrations that resulted in crack formation under repeated cyclic loadings, leading to the through crack which propagated by corrosion fatigue.

14. Conclusions

1. Visual examination revealed that the part exhibited beach marks indicative of a fatigue failure. Also, regions of inter-granular attack were noted on the exterior surface of the bearing adjacent to the origin. This attack was only noted on the exterior surface of the component.

2. The composition of the part met the requirement of type 440C stainless steel per AMS 5630.

3. Metallography confirmed the presence of inter-granular attack along the exterior of the component. The etched structure was consistent with this alloy undergoing a similar heat treatment and exhibiting blocky primary carbides, as well as small spheroidal secondary carbides.

4. The hardness of the component (as well as the outer ring and main body) met the drawing requirements.

5. Micro-hardness testing showed that no surface anomaly such as decarburization existed.

6. SEM was used to further characterize the inter-granular surface attack, as well as the morphological features of the fracture surface. EDS was used to identify the elements within the corroded fracture surface.

7. Retained austenite measurements of the component revealed readings that were well within the governing requirement.

8. The part was determined not to be sensitized, when subjected to testing outlined in Specification HP 1-1.

15. Recommendations

As shown in table 15, type 440C steel is susceptible to corrosion in industrial, marine, and salt water environments. It also corrodes readily when in contact with mild, oxidizing, and reducing chemicals. Based on this, care should be taken to avoid prolonged exposure to these environments, which may promote corrosion attack of this alloy. Until recently, type 440C offered an unmatched combination of high hardness, excellent wear properties and mild atmosphere/fresh water corrosion resistance. However, the development of new alloys promises to rival type 440C in these areas and may warrant future consideration. Although the replacement of type 440C alloy with another alloy may not be feasible if this failure were an isolated incident, future consideration should be given to a number of alloys if this is a recurring problem. One alloy developed in Japan purportedly has increased corrosion resistance and improved life expectancy and surface finish (*9*). The advantages were attributable to the absence of large primary carbides in the quenched and tempered microstructure, which shorten bearing life. The material, designated DD400, is austenitized and quenched in a vacuum furnace and then refrigerated to subzero temperatures to transform the most possible austenite to martensite. Maximizing the level of undissolved chromium in the austenite and eliminating primary carbides enhances the corrosion performance. The microstructure of DD400 contains only secondary carbides in the tempered martensitic structure. Faster quench rates, as well as lower carbon and chromium levels favor the development of the fine secondary carbides. This material is being produced in the United States by Mineba NMB[5] USA, Inc., Chatsworth CA, 818-341-0820. In addition, Latrobe Steel, Latrobe, PA, 724-532-6521, has developed two alloys that are purportedly superior to type 440C with respect to corrosion resistance and metal-to-metal wear, designated CSS[6]-42L and 440N-DUR, respectively (*10*). The CSS-42L alloy is a double vacuum melted alloy with a nominal composition of 0.12 C, 14.0 Cr, 2.0 Ni, 12.0 Co, 4.75 Mo, 0.6 V, and 0.02 Nb and was designed for bearing applications. The 440N-DUR martensitic stainless steel alloy was designed to provide hardness and corrosion resistance superior to type 440C,

[5]not an acronym

[6]CSS and DUR are internal designations by Latrobe.

while reducing the carbide size and providing for more uniform carbide distribution. Alloy 440N-DUR is an air-melted alloy with a nominal composition of 0.66 C, 14.5 Cr, and 0.100 N. The nitrogen combined with the carbon and chromium improves the "hardenability" and corrosion resistance (*11*). Finally, an alloy designated Cronidur 30 is purported to have 100 times the corrosion life of type 440C and 5 times the bearing life of M50 steel (*12*). The nominal composition of this alloy is 0.31 C, 0.38 N, 0.55 Si, 15.2 Cr, and 1.02 Mo. The alloy possesses a combination of properties that meet all bearing requirements including adequate hardness, high wear resistance, good fracture toughness, and excellent corrosion resistance. This alloy does not contain any coarse carbide stringers that would increase the strength, ductility, and fatigue resistance.

16. References

1. Magee, J. Personal communication, Carpenter Specialty Steels, Reading, PA, 19 August 1998.
2. Wulpi, D.J. *Failures of Shafts and Bearings*; ASM Case History, Course 13, Lesson, Test 11; A Lesson From *Principles of Failure Analysis,* pp 25-26, 1985.
3. Kraus, G. *ASM Principles of Heat Treatment*, p. 230, 1980.
4. Alloy Digest, Inc. AISI Type 440C, Filing Code SS-101, In *Alloy Digest*, Orange, NJ, revised June 1988.
6. American Society of Metals, *Stainless Steel*, Volume 3, Ninth Edition, Wrought Stainless Steels, p.11, 1980.
7. ASM Specialty Handbook, *Stainless Steels*, Tribological Properties, 1994, p. 533.
8. ASM *Properties and Selection: Irons, Steels and High-Performance Alloys*, Volume 1, Tenth Edition, Wrought Stainless Steels, 1990, p. 873.
9. Rideout, J. *Advanced Materials & Processes,* ASM Technical Spotlight, Bearing Steel Bests Type 440C, 12/92, pp. 39-40.
10. Tomasello, C.M. *Advanced Materials & Processes*, ASM Technical Spotlight, Aerospace Bearing and Gear Alloys, pp 59-61, July 1998.
11. Tomasello, C.M.; Maloney, J.L.; Ward, P.C.; Materkowski, J.P. A New Corrosion-Resistant, Martensitic Stainless Steel for Improved Performance in Miniature Bearings. *Bearing Steels: Into the 21st Century*, ASTM STP 1327, p. 437, 1998.
12. Trojahn, W.; Streit, E.; Chin, H.A.; Ehlert, D. Progress in Bearing Performance of Advanced Nitrogen Alloyed Stainless Steel, Cronidur 30, *Bearing Steels: Into the 21st Century*, ASTM STP 1327, p. 447, 1998.
13. American Society for Testing Materials. *Book of Standards*; ASTM-E-975, Vol. 03.01; ASTM: West Conshohocken, PA, 2000.

Appendix A. Corrosion and Wear Resistance of Various Stainless Steel Alloys

Table A-1. Comparison of the resistance of standard types of stainless steel to various classes of environments (taken from ASM Metals Handbook (*6*))

Type	Mild atmospheric and fresh water	Atmospheric		Salt water	Chemical		
		Industrial	Marine		Mild	Oxidizing	Reducing
Austenitic stainless steels							
201	x	x	x		x	x	
202	x	x	x		x	x	
205	x	x	x		x	x	
301	x	x	x		x	x	
302	x	x	x		x	x	
302B	x	x	x		x	x	
303	x	x			x		
303Se	x	x			x		
304	x	x	x		x	x	
304H	x	x	x		x	x	
304L	x	x	x		x	x	
304N	x	x	x		x	x	
S30430	x	x	x		x	x	
305	x	x	x		x	x	
308	x	x	x		x	x	
309	x	x	x		x	x	
309S	x	x	x		x	x	
310	x	x	x		x	x	
310S	x	x	x		x	x	
314	x	x	x		x	x	
316	x	x	x	x	x	x	x
316F	x	x	x	x	x	x	x
316H	x	x	x	x	x	x	x
316L	x	x	x	x	x	x	x
316N	x	x	x	x	x	x	x
317	x	x	x	x	x	x	x
317L	x	x	x	x	x	x	x
321	x	x	x		x	x	
321H	x	x	x		x	x	
329	x	x	x	x	x	x	x
330	x	x	x	x	x	x	x
347	x	x	x		x	x	
347H	x	x	x		x	x	
348	x	x	x		x	x	
348H	x	x	x		x	x	
384	x	x	x		x	x	
Ferritic stainless steels							
405	x				x		
409	x				x		
429	x	x			x	x	
430	x	x			x	x	
430F	x	x			x		
430FSe	x	x			x		
434	x	x	x		x	x	
436	x	x	x		x	x	
442	x	x			x	x	
446	x	x	x		x	x	
Martensitic stainless steels							
403	x				x		
410	x				x		
414	x				x		
416	x						
416Se	x						
420	x						
420F	x						
422	x						
431	x	x	x		x		
440A	x				x		
440B	x						
440C	x						
501							
502							
503							
504							
Precipitation-hardening stainless steels							
PH 13-8 Mo	x	x			x	x	
15-5 PH	x	x	x		x	x	
17-4 PH	x	x	x		x	x	
17-7 PH	x	x	x		x	x	

An "x" notation above indicates that the specific type is considered resistant to the corrosive environment.

Table A-2. Comparison of the adhesive wear resistance of standard types of stainless steel (taken from ASM Specialty Handbook (*7*))

Alloy	Rockwell hardness	Volume loss, mm^3		
		10,000 cycles(a), at 100 rev/min	40,000 cycles at 100 rev/min	40,000 cycles at 400 rev/min
Austenitic stainless steels				
Type 201	93.0 HRB	3.2	10.9	7.4
Type 304	78.0 HRB	10.4	23.5	22.0
Type 304	98.0 HRB	13.6	30.0	27.0
Type 304 HN	91.5 HRB	12.5	44.4	19.5
Type 304 HN	22.5 HRC	12.7	45.4	23.7
Type 301	90.0 HRB	6.9	...	...
Type 316	91.0 HRB	15.8	...	...
Type 303	98.0 HRB	488.7	...	...
S20161	96.0 HRB	1.3	5.3	4.4
S20161	30.0 HRC	1.5	5.5	4.5
S20910	96.0 HRB	11.7	46.0	16.7
S21000	88.0 HRB	12.0	43.8	9.9
S21800	93.0 HRB	4.2	12.1	5.2
S21900	92.0 HRB	11.9	45.0	34.1
S24100	95.5 HRB	7.2	21.9	5.2
S28200	99.0 HRB	8.1	27.9	2.8
S28200	35.0 HRC	7.5	22.5	2.7
S30430	72.0 HRB	18.2	42.8	29.1
N08020	87.5 HRB	22.6	84.3	28.2
Other stainless steels				
Type 410	24.5 HRC	114.0	544.0	251.1
Type 410	39.0 HRC	215.0	632.0	93.8
S42010	49.5 HRC	96.9	115.7	8.1
S42010	47.0 HRC	178.6	680.3	35.7
Type 420	50.5 HRC	83.8	84.0	8.5
Type 420	46.0 HRC	215.0	...	...
Type 440C	56.0 HRC	0.7	1.3	1.1
Type 440C	26.5 HRC	44.1	191.0	38.8
S17400	30.5 HRC	83.0	281.3	53.0
S17400	40.0 HRC	50.8	202.8	45.7
S13800	32.5 HRC	77.5	...	...
S13800	47.0 HRC	49.1	...	...
Type 431	42.0 HRC	235.6	...	...
Type 430	76.5 HRB	52.4	194.6	133.9
Type 430	80.5 HRB	58.5	229.7	171.6
S32950	23.0 HRC	15.8	50.5	22.5

Note: Based on crossed-cylinder wear test, ASTM G 83, 71 N (16 lbf). (a) Procedure A

NO. OF
COPIES ORGANIZATION

* ADMINISTRATOR
DEFENSE TECHNICAL INFO CTR
ATTN DTIC OCA
8725 JOHN J KINGMAN RD STE 0944
FT BELVOIR VA 22060-6218
*pdf file only

1 DIRECTOR
US ARMY RSCH LABORATORY
ATTN AMSRL CI IS R REC MGMT
2800 POWDER MILL RD
ADELPHI MD 20783-1197

1 DIRECTOR
US ARMY RSCH LABORATORY
ATTN AMSRL CI OK TECH LIB
2800 POWDER MILL RD
ADELPHI MD 20783-1197

1 DIRECTOR
US ARMY RSCH LABORATORY
ATTN AMSRL D D SMITH
2800 POWDER MILL RD
ADELPHI MD 20783-1197

ABERDEEN PROVING GROUND

2 DIRECTOR
US ARMY RSCH LABORATORY
ATTN AMSRL CI OK (TECH LIB)
BLDG 305 APG AA

10 DIRECTOR
US ARMY RSCH LABORATORY
ATTN AMSRL WM MD S GRENDAHL
BLDG 4600